NTNU

Norwegian University of
Science and Technology

# Adaptive Clutter Filtering for Improved Measurement of Cardiac Blood Velocities

Beate Haram Vågsholm

Master of Science in Physics and Mathematics
Submission date: June 2017
Supervisor: Rita de Sousa Dias, IFY
Co-supervisor: Lasse Løvstakken, ISB
Solveig Fadnes, ISB

Norwegian University of Science and Technology
Department of Physics

# Forbedre visualiseringen av blodstrømmer i hjertet ved å bruke adaptiv filtrering

I ultralyd fargedoppler kan atypiske blodstrømmer være en tidlig indikasjon på hjertefeil. Blodstrømmen kan også visualiseres med teknikker for flerdimensjonal blodstrømsestimering som *speckle tracking*. For å kunne visualisere blodstrømmen må signalet fra det omkringliggende vevet dempes, dette er ofte kalt *clutter-filtrering*. Om vevssignalet ikke er tilstrekkelig dempet kan dette føre til bias i hastighetsmålingene.

For avbildinger av hjertet er det vanskelig å bruke filtre med én fast cutoff-frekvens fordi blod- og vevshastighetene endrer seg i løpet av hjertesyklusen. Én mulig løsning for å unngå blinkende vev, og tap av blodsignal er å bruke adaptive filtre. Eigenverdi-regresjonsfiltre er én type adaptive filtre, og i dette arbeidet ble det undersøkt om clutter filtrering av ultralyddata fra hjerte er enda en passende applikasjon for eigenverdi-regresjonsfiltre.

Valg av clutter-delmengden er utfordrende med eigenverdi-regresjonsfiltre. I dette arbeidet ble clutter-delmengden valgt manuelt, ved å benytte en tidligere foreslått halvautomatisk metode, og ved å benytte to helautomatiske metoder.

Datasettene som ble analysert under arbeidet var *in vivo* data og simuleringer. Eigenverdi-regresjonsfilteret med manuelt valg av clutter-delmengden kan forbedre visualiseringen av virveldannelsen i blod sammenlignet med et konvensjonelt filter for hjertedata. Men forbedringen var ikke evaluert av klinikere og bare fem ulike bilder ble vurdert. Disse bildene var fra tre ulike datasett. Eigenverdi-regresjonsfilteret kan gi lavere bias i hastighetsestimeringene fra speckle tracking, siden det kan redusere blinking av vev og hindre tap av blodsignal. Dette ble undersøkt ved å gjøre enkle simuleringer.

Den halvautomatiske metoden valgte riktigst clutter-delmengde av de tre metodene som ble undersøkt i dette arbeidet. Den var riktig i 44 % av tilfellene i diastole, men bare ett bilde hver, fra ni ulike datasett ble undersøkt. Den halvautomatiske metoden er ikke en praktisk løsning siden en region i bildet som inneholder vevssignal og en som inneholder blodsignal må velges manuelt.

# Preface

This master thesis in Ultrasound technology as part of the study program Biophysics and medical technology is a continuation of the project work carried out during autumn 2016 in the course TFY4500 - Biophysics, Specialization Project. This master thesis was written during the spring semester of 2017. It was in cooperation with the Department of Circulation and Medical Imaging at St. Olavs Hospital. The idea to the prosject was brought up during a project work presentation febuary 2016 for students taking the course TTK4165 Signal Processing in Ultrasound Imaging. It is intended to be used in a larger project where the overall aim is to use speckle tracking and color flow imaging for blood velocity estimation as an aid in diagnosing heart disease in infants.

The assumed background of the readers of this report is master students in their last year in study program Biophysics and medical technology.

Trondheim, 2017-06-11

Beate Haram Vågsholm

# Acknowledgment

I would like to thank Solveig Fadnes, Lasse Løvstakken, Ingvill Kinn Ekroll, Cristiana Golfetto, Hans Torp, Jørgen Avdal, Morten Smedsrud Wigen and Rita de Sousa Dias for their great help during my master thesis.

B.H.V.

# Summary and Conclusions

In ultrasound color flow images of the heart, irregular blood flow patterns might be an early indication of heart disease. The blood flow is possible to image using multi-dimensional blood velocity estimation like speckle tracking. In order to image the blood flow the signal from the surrounding tissue must be attenuated, and this is often termed clutter filtering. Insufficient clutter filtering might cause bias in the velocity estimation.

It is difficult to design filters with a fixed cut-off frequency for cardiac imaging since the blood and clutter velocity changes during the heart cycle. A possible solution to avoid both tissue flashing and blood signal drop-out is to use adaptive filters. Eigenvalue regression filters are one type of adaptive clutter filters, and in this project it was investigated if clutter filtering of cardiac data was yet an other suitable application for eigenvalue regression filters.

Selection of a clutter subspace is a challenge when using eigenvalue regression filters. In this work the clutter subspace was chosen manually, and by using a previous suggested semi-automatic approach, and two fully automatic approaches.

Analyzed datasets included *in vivo* data, and simulations. The eigenvalue regression filter with a manually selected clutter subspace has the possibility of improving the visualization of vortex formation in blood compared to a conventional filter for cardiac data. However, the improvement was not judged by clinicians, and only five different frames were considered. These frames were from three different *in vivo* datasets. The results from the simple simulations showed that the eigenvalue regression filter can reduce the bias in the velocity estimate from speckle tracking compared to a FIR filter, as it reduces tissue flashing, and blood signal drop-outs.

The semi-automatic approach select the clutter subspace most correctly out of the three methods considered in this work. It was correct in 44 % of the frames in diastole, but only one frame from nine different datasets were considered. The semi-automatic approach is not a practical solution since a region containing clutter and blood signals must be chosen manually.

The report is structured as follows. Chapter 1.1, the introduction, contain clinical motivation, and an overview of some previously purposed adaptive clutter filters. It also include the problem formulation, the objectives, limitation and approach for this work. Chapter 2 intro-

duces the estimators and conventional filters commonly used in color flow imaging. Following, the eigenvalue regression filter is thoroughly explained. The Nyquist velocity for pulsed wave Doppler is defined, and some image artefacts in color flow imaging are presented. A brief summary of multi-dimensional blood velocity estimation is given, focusing on speckle tracking. The chapter ends with a short explanation of the sonogram.

Chapter 3 gives details regarding the data aquisition, the simulations, and the post processing of the data. It explains how the spectral content was estimated. It also explaines how the eigenvalue regression filter was implemented, and some methods for selecting the clutter subspace automatically. The last subsection gives detail regarding the parameters used for the speckle tracking. The *in vivo* data that has been analyzed in this project is presented in table 3.1, and the simulations in table 3.2.

The results are presented in chapter 4 and are structured by objective, followed by chapter 5 which includes a discussion of the results. The report ends with chapter 6, the conclusion, and suggestions to further work.

# Contents

# Chapter 1

# Introduction

## 1.1 Background

Congenital heart disease is the most common birth defect and affects about 1 % of all live births, van der Linde et al. (2011). Such diseases may affect the blood flow, causing irregular vortex formation in the heart. This might alter the pressure distribution, and can contribute to an extra load for the heart muscle. Untreated, this may cause abnormal growth of the heart muscle or heart failure.

In diastole when the ventricles are filled, there is a vortex flow of blood in the left ventricle in an healthy heart. Figure 1.1, Pedrizzetti et al. (2014), shows the blood flow in an healthy heart to the left, next to a heart with impaired flow. It also shows how impaired flow might lead to dilatation of the heart. The pressure gradient, shown in arrows, is longitudinal in the healthy heart. In the heart with impaired flow there is both a longitudinal and transversal pressure gradient, and the dilatation of the heart is a reaction to the transversal pressure gradient.

Prenatal diagnosis of congenital heart disease has been shown to lead to a variety of favorable outcomes, listed below.

- Significant decrease in postnatal morbidity in infants with left heart obstructive lesions Eapen et al. (1998).
- Has a favorable impact on treatment of patients who have hypoplastic left heart syndrome, and are undergoing staged palliation and reduces early neurologic morbidity Mahle et al. (2001).

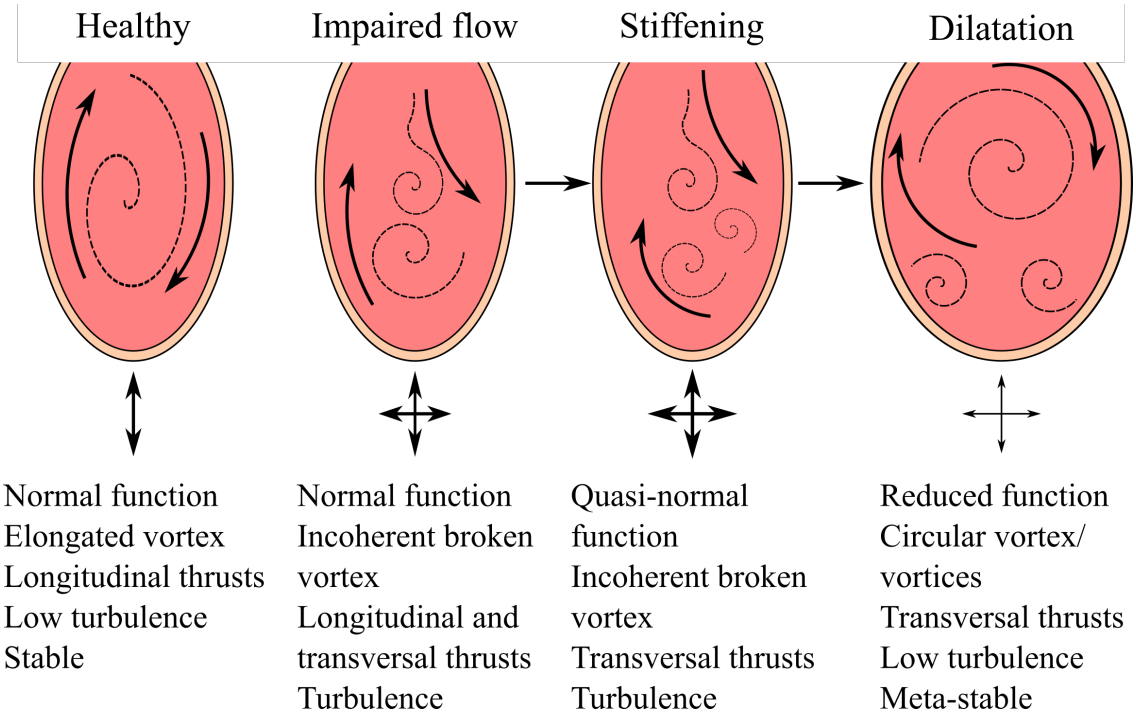


Figure 1.1: Figure from article by Pedrizzetti et al. (2014), showing how a transversal pressure gradient in impaired flow might cause dilatation of the heart. Gray arrows indicate the components of the pressure gradient.

- Minimizes metabolic acidosis in patients and may be associated with improved long-term outcome and prevention of cerebral damage Verhejien et al. (2001),
- Was associated with a decreased need for invasive respiratory support Landis et al. (2013).

Some other studies have found that neonatal and postnatal diagnosis of congenital heart disease is less favorable. The setting in which neonatal congenital heart disease is first recognised has an impact on preoperative condition, which in turn influences postoperative progress and survival after surgery, Brown et al. (2006). In addition postnatal diagnosis of pulmonary atresia, another type of congenital heart disease, is associated with greater cyanosis at presentation, Tzifa et al. (2007).

Some conventional methods in ultrasound tecnology that are used in prenatal diagnosis of congenital heart disease are B-mode (grayscale two-dimensional echocardiography), M-mode, spectral Doppler (pulsed wave and continous wave) and color flow imaging (color coded two-dimensional Doppler echocardiography), Achiron et al. (1992), Rajiah et al. (2011), Yagel et al. (1997). Ultrasound technology is used for detection of congenital cardiac anomalies, but there

are still reported undetected defects and misdiagnosis, Benavidez et al. (2008).

In color flow imaging, blood velocities are shown in a colormap on top of a grayscale (B-mode) image showing the structures of the heart. The signal contain signals from thermal noise, tissue signals which are often called the clutter signal, and blood signal. The clutter signal is usually much stronger than the blood signal and has to be attenuated to achieve high quality color flow images.

The current method of distinguishing between the different signals; blood and clutter, is to use a high pass filter that should attenuate the clutter signal with low velocity, while the blood signal with high velocity should fall within the passband. Previous research in color flow imaging has shown that polynomial regression filters are suitable as clutter filters because they have a sharp transition region when few samples are available for filtering. Also, for frequencies in the passband, a polynomial regression filter has a negligible influence on the bias and standard deviation of the mean frequency estimate, which is used in calculation of the color flow, Bjærum et al. (2002b).

It systole the mitral valve closes, the ventricle contract and blood flows out through the aortic valve. In the end of the diastole and the beginning of the systole the velocity of both clutter and blood signal is low, and in some cases the blood spectrum falls below the cut-off frequency of the filter and is attenuated together with the clutter signal. As a result, blood will not show up in the image, making it difficult to estimate the true blood flow pattern, and visualize the vortex formation in the blood flow. Accelerated clutter or otherwise clutter with high velocities might fall within the passband of the filter and show up as tissue flashing, or contribute to biased velocity estimates. The heart valve is especially difficult to remove from ultrasound images of apical views of the heart with conventional high-pass filters. A possible solution to avoid both tissue flashing and blood signal drop-out is to use filters with an adaptive cut-off frequency.

Previously purposed adaptive clutter filters include downmixing filters and eigenvalue regression filters. Eigenvalue regression filters are an other type of regression filters that uses a basis calculated using a Karhunen-Loève transform. This transform has the property that the clutter representation is optimum and therefore this filter is a regression filter with an optimal signaldependent set of basis vectors, and the maximum amount of clutter energy is removed from the signal, Bjærum and Torp (1997), Ledoux et al. (1997), Bjærum et al. (2002a). For B-

mode images of *in vivo* scenarios with substantial clutter motion eigenvalue regression filters improve the contrast between clutter and blood compared to using polynomial regression filters. The *in vivo* data examples include intra-operative coronary imaging and thyroid imaging. And a frequency-based algorithm was used to select the clutter subspace for the eigenvalue regression filter, Yu and Løvstakken (2010). The eigenvalue regression filter can also be used for applications with low blood velocity if the packet size is high, i. e. $N_p = 100$ and the pulse repetition frequency ($PRF$) is high 5−10 kHz. However it is not suited for color flow imaging if the blood velocity is low, Ledoux et al. (1997). Eigenvalue regression filters can improve the visualization of small blood vessels with low blood velocities, like microvascular networks, Demené et al. (2015).

It has also been shown that adaptive filters improves the image quality when imaging small vessels in the thyroid gland. The cut-off frequency for the filter remained fixed, and the signal were downmixed by varying phase increments. The downmixing approach allowed for adaption to accelerating clutter movement. The phase increments were calculated from the autocorrelation function of the unfiltered data. The downmixing approach outperformed both the polynomial regression filter and the eigenvalue regression filter for this application, Bjærum et al. (2002a).

Problem formulation: Improve the estimation of intracardiac flow patterns using adaptive clutter filtering.

When using the eigenvalue regression filter the clutter subspace is subtracted from the signal. The clutter subspace consist of an unknown number of the most dominant eigenvectors. Different methods have been purposed to select the clutter subspace automatically. Yu and Løvstakken (2010) suggest calculating the power of the eigenvalues and the Doppler velocity of the eigenvectors, and setting predefined power and Doppler velocity threshold values. Faurie et al. (2017) suggest considering the 30% eigenvalues with highest power as the clutter, and removing the corresponding eigenvectors. Demené et al. (2015) suggest either using the power of

the clutter and blood signal to set a threshold value, or setting a predefined number of the eigenvectors with highest power as the clutter subspace, and letting the clinician decide the clutter subspace for the current application and data.

Some fully automated approaches to set an adaptive threshold value for the eigenvalue regression filter include minimax Donoho and Gavish (2014), robust principal component analysis (PCA) Candès et al. (2005), Akaike information criterion (AIC) or the minimum description length (MDL) Allam et al. (1996) Wax and Kailath (1985), and dynamic mean evaluation Fort et al. (1995). Details regarding these methods are given in section 3.4. For the robust PCA, AIC and MDL, each possible maximum eigenvalue for the blood subspace is considered and a cost function is calculated. The threshold is set by finding the minimum of the cost function.

During diagnosis it is important that the velocity estimates are accurate and the methods for estimation are robust, so that the diagnosis is not based on a flawed dataset. To increase accuracy of the adaptive filtering method, the following problems remains to be accessed. Get input from clinicians to determine if the visualization of the blood vortex in this application is improved when filtering with the eigenvalue regression filter. Simulations with an expanding phantom for even better understanding of the fundamental properties of the eigenvalue regression filter, and to give more information in order to develop a robust method for clutter subspace selection. Develop a method to also select a velocity threshold, and a method to select a power threshold without the need for an input. Evaluation of which of the aforementioned methods yields the most accurate clutter subspace, and is the most practical in the sense that it is not too computer intensive. Consideration of machine learning and image recognition algorithms to select clutter subspace based on plots of eigenvalue power and spectral content, and in terms of computer complexity, how it would perform compared to the aforementioned methods for clutter subspace selection. Compare the eigenvalue regression filter and the downmixing filter for this application.

## 1.2 Objectives

The main objective of this project is to improve the estimation of intracardiac flow patterns using adaptive clutter filtering.

The secondary objectives are to

1. Investigate the potential of adaptive eigenvalue regression filter in cardiac imaging
2. Investigate the fundamental properties of the eigenvalue regression filter for separating blood and clutter signal
3. Investigate the possibility of adaptive basis order selection in the eigenvalue regression filter

## 1.3 Limitations

In this master thesis the eigenvalue regression filter was applied as a clutter filter for cardiac data. Only ultrasound data of apical views of the left ventrical were considered. In the heart the blood flow has complex patterens. And, when measuring the Dopplershift of the blood, only the frequency shift of the axial velocity component is measured. The loss of the velocity component perpendicular to the ultrasound pulse makes it difficult to accurately estimate the blood flow pattern in the heart.

The application of eigenvector filters for use with color flow and speckle tracking was evaluated compared to a FIR filter and a polynomial regression filter with fixed order, and the downmixing filter was not considered. Only quantitative examples are presented when comparing the visualization of the vortex when filtering with the eigenvalue regression filter and the FIR filter. This was only done for three of the *in vivo* datasets. For the visualization of the blood vortex with speckle tracking estimates the averaging region in both space and time was considered large.

## 1.4 Approach

The adaptive filter used in this work was an eigenvalue regression filter. To investigate the potential of the eigenvalue regression filter in cardiac imaging, *in vivo* data is used. Firstly, the clutter signal for cardiac data is analyzed over time. Diastole and systole are determined by inspection of the sonogram, B-mode images, and color flow images for different time points during

the heart cycle. The frequency spectrum is calculated for a region in the lumen, in the heart wall, and in the ventricular septum. This is done for different times during diastole and plotted together with the frequency spectrum for the blood flow imaging (BFI) finite impulse response (FIR) filter.

To investigate how the signals contained in the different eigenvectors are distributed in space, the projection of each eigenvector is shown as a B-mode image. The power of the eigenvalues are also plotted against the Doppler velocity of its corresponding eigenvector. This is done for a frame in systole, and diastole for two dataset with different $PRF$. To investigate how the signals contained in the different eigenvectors are distributed in frequency, the power distribution of the spectral content of the eigenvectors, are shown for a frame in systole and diastole for different filter basis sizes. In order to visualize the intracardiac flow patterns speckle tracking was used. The eigenvalue regression filter was compared to the conventional FIR filter, and the clutter subspace was chosen manually for the eigenvalue regression filter. Quantitative examples from the speckle tracking for the two cases are shown. These examples are from three different *in vivo* datasets.

To investigate the fundamental properties of the eigenvalue regression filter for separating blood and clutter signal, simulations are used. This is done as a first step in order to develop a robust fully automatic approach for selecting the clutter subspace. The simulations are simple with two different constant velocities. They are used to determine how the velocity difference between two constant velocities affect the eigenvalue regression filter performance. One velocity, simulating the clutter velocity, was kept constant for all simulations and the other, simulating blood, was varied. Two cases are considered in more depth, one with a small velocity difference between clutter and blood, and one with a large difference. For these simulations the eigenvalues are plotted and compared to the case with only clutter velocity. For these two cases, and the case with only clutter signal, the spectral content of the eigenvectors are imaged as a colormap showing the power distribution. For four different simulations with increasing difference in blood and clutter velocity the signal clutter ratio (SCR) is calculated and plotted for packet size one to sixty four. These plots are compared to similar plots from one of the *in vivo* datasets.

Simulations are used to compare the eigenvalue regression filter to two conventional filters,

the polynomial regression filter, and a FIR filter. The simulation parameters is chosen as the maximum absolute velocity for clutter, and blood, for a frame in systole, and a frame in diastole, for dataset *Testdata2*. The velocities is found by inspection of the sonogram. The absolute velocity was determined from the blood flow in a video of B-mode images, and was found to be the same as the axial velocity for those frames. For the FIR filter and the eigenvalue regression filter the bias and the standard deviation of the velocity estimates from speckle tracking was calculated, and examples from the speckle tracking is shown.

To investigate the possibility of adaptive basis order selection in the eigenvalue regression filter, *in vivo* data is used. Three previously purposed methods to select the clutter subspace is evaluated for a frame in systole, and a frame in diastole, for nine different *in vivo* datasets. These methods are compared to the clutter subspace chosen manually. The clutter subspace was chosen manually by inspection of the B-mode images of the different eigenvectors.

# Chapter 2

# Theory

Color flow imaging is a medical imaging modality where the mean axial velocity of blood flow is estimated using ultrasound Doppler. The estimated velocity for a region-of-interest (ROI) is displayed as a colormap ranging from red to blue, for positive and negative velocities. The color flow image is usually superimposed with a B-mode ultrasound image showing the tissue structure, Reid and Spencer (1972) Ferrara and DeAngelis (1997). In color-flow imaging the time dimension is divided into slow-time and fast-time. The slow-time dimension is used for filtering and is often termed packet. It consist of $N_p$ consecutive pulses. The fast-time dimension is the depth dimension.

## 2.1 Estimators in Color Flow Imaging

In color flow imaging the mean Doppler frequency is estimated using the autocorrelation function $\hat{R}_x(m)$ in the packet dimension. The autocorrelation function $\hat{R}_x(m)$ with packet size $N_p$ and lag $m$ for a Doppler signal $x$ from a given spatial sample, is given by

$$\hat{R}_x(m) = \frac{1}{N_p - 1} \sum_{n=0}^{N_p-2} x(n)^* x(n+m). \tag{2.1}$$

An estimator for the blood signal power is given by the autocorrelation function with lag equal to zero, $\hat{P} = \hat{R}_x(0)$.

For two subsequent temporal samples, the movement of a scatterer introduces a phase dif-

ference between the signals. This phase difference is estimated using the autocorrelation $\hat{R}_x(m)$ with lag equal to one, and it gives an estimator for the mean Doppler frequency in the axial direction $\hat{\bar{\omega}} = \angle\hat{R}_x(1)$, Kasai et al. (1983). The mean axial velocity $\hat{v}_{\text{axial}}$ is calculated from this estimator as

$$\hat{v}_{\text{axial}} = \frac{c \cdot PRF}{4\pi f_0}\angle\hat{R}_x(1) \tag{2.2}$$

where $PRF$ is the pulse repetition frequency, $f_0$ is the center frequency of the emitted ultrasound pulse, and $c$ is the velocity of sound in tissue.

Turbulence in the blood flow is often indicated as a green hue in the color flow image. The blood flow is often considered turbulent if the bandwidth is large. An estimator for the bandwidth $\hat{B}^2$ depends on the estimate of the blood signal power $\hat{P}$ and the estimate of the mean Doppler frequency $\hat{\bar{\omega}}$. An overview of these three common estimators in color flow imaging is given by

$$\hat{P} = \hat{R}_x(0) \quad \hat{\bar{\omega}} = \angle\hat{R}_x(1) \quad \hat{B}^2 = 1 - \frac{|\hat{R}_x(1)|}{\hat{R}_x(0)}. \tag{2.3}$$

## 2.2 Clutter Filtering in Color Flow Imaging

The received signal in color flow imaging is considered a superposition of signals arising from moving clutter, moving blood and thermal noise. In order to image the blood signal it is necessary to attenuate the signal from moving clutter. It is well known that the clutter signal power is about 40-100 dB stronger than blood, and would otherwise hide the blood signal.

Filtering is done in the packet dimension and the packet size is determined by the depth of the ROI and the frame rate. For cardiac imaging these two conditions result in one packet consisting of only eight to sixteen temporal samples. The order of the filter is limited to the size of the packet. This further limit the possibility of designing sharp clutter filters with a narrow transition region.

Two conventional clutter filters in color flow imaging are polynomial regression filters, and FIR filters. The polynomial regression filter is suitable for clutter filtering in color flow imaging because it has a narrow transition region for low packet sizes Bjærum et al. (2002b). FIR filters has the advantage that they can be designed to be time-invariant. For time-invariant filters the Doppler signal waveform is not distorted from filtering.

### 2.2.1 FIR Filter

The output of a FIR filter can be described by a finite convolution sum as

$$y(n) = \sum_{k=0}^{K-1} h(k)x(n-k) = \sum_{k=n-K+1}^{n} h(n-k)x(k) \tag{2.4}$$

for a FIR filter of order $K-1$. The number of valid output samples are $N-K-1$, and the first $K-1$ output samples have to be discarded because of the filter initialization.

### 2.2.2 Polynomial Regression Filter

When using a polynomial regression filter the clutter component is subtracted from the signal. The clutter component is modelled using a Legendre polynomial base, and is the signal component contained in a $K_c$ dimensional space. The filter output $\mathbf{y}$ is given by

$$\mathbf{y} = (\mathbf{I} - \sum_{k=0}^{K_c-1} \mathbf{b_k}\mathbf{b_k}^{*\mathbf{T}})\mathbf{x} = \mathbf{A}\mathbf{x} \tag{2.5}$$

where the input signal vector $\mathbf{x}$ is projected onto the complement of the clutter component basis. The term $\mathbf{b_k}$ are orthonormal basis vectors spanning the clutter signal subspace, $\mathbf{I}$ is the identity matrix and $\mathbf{A}$ is a projection matrix, Torp (1997), Hoeks et al. (1991).

The QR factorization of matrix $\mathbf{A}$ can be calculated from a Householder reflection, which is a transformation that takes a vector and reflects it about some plane, Trefethen (2008).

## 2.3 Eigenvalue Regression Filter

An estimator for the signal power is obtained from the correlation matrix $\hat{\mathbf{R}}_x(0)$ as previously noted in section 2.1. Since the signal is assumed to be a superposition of signals arising from blood, tissue and noise, the correlation matrix can be written according to

$$\hat{\mathbf{R}}_x(0) = \hat{\mathbf{R}}_c(0) + \hat{\mathbf{R}}_b(0) + \sigma_n^2\mathbf{I}. \tag{2.6}$$

Where $\hat{\mathbf{R}}_c(0)$ is the correlation matrix of the clutter signal, and $\hat{\mathbf{R}}_b(0)$ is that of the blood signal. The noise is assumed to be white, and therefore it has a constant value equal its variance.

This correlation matrix can be considered a linear combination of orthonormal basis vectors if the signal vector $\mathbf{x}$ is expanded into the basis given by

$$\hat{\mathbf{R}}_x(0) = E\{\mathbf{x}\mathbf{x}^{*T}\} = \sum_k \lambda_k \mathbf{e}_k \mathbf{e}_k^{*T}. \tag{2.7}$$

This expansion, called a principal component analysis (PCA) Pearson (1901), the Hotelling transform, or the discrete Karhunen-Loève transform (DKLT) Therrien (1992), yields the orthonormal eigenvectors $\mathbf{e}_k$ of the correlation matrix. The power of each eigenvector is given by its eigenvalue $\lambda_k$, and the total energy in the signal is equal to the sum of the eigenvalues. The eigenvalue distribution is therefore a measure of the bandwidth of the signal, Bjærum et al. (2002a).

In order to calculate the eigenvalues and eigenvectors the correlation matrix $\hat{\mathbf{R}}_x(0)$ should be a full rank matrix, so that each row of equations is independent. The correlation matrix has full rank if the number of spatial samples is at least equal to the packet size.

The filtered signal $\mathbf{y}$ is given by

$$\mathbf{y} = (\mathbf{I} - \sum_{k=0}^{K_c-1} \mathbf{e}_k \mathbf{e}_k^{*T})\mathbf{x} \tag{2.8}$$

where $\mathbf{I}$ is the identity matrix, $\mathbf{e}_k$ is eigenvector number $k$, and the sum corresponds to the clutter subspace, and $\mathbf{x}$ is the input signal vector. The eigenvectors are calculated from the correlation matrix $\hat{\mathbf{R}}_x(0)$ of the packet dimension as in equation 2.7, Yu and Løvstakken (2010).

The eigenvector regression filter is inherently adaptive because the expansion is carried out in the packet dimension and is done independently for each frame. This way, each frame will have unique eigenvalues and eigenvectors that are the best fit to the motion at that time.

The main idea of the eigenvector regression filter is to subtract the clutter signal represented as the $K_c$ eigenvectors with the highest power. Figure 2.1 is an illustration of this idea. This is challenging when there are more than one clutter component and when the clutter components have different velocities. Then the clutter signal is no longer only present in the most dominant eigenvector, but might be spread across an unknown number of eigenvectors.

To properly supress the clutter signal, the clutter and blood signals must be mostly con-

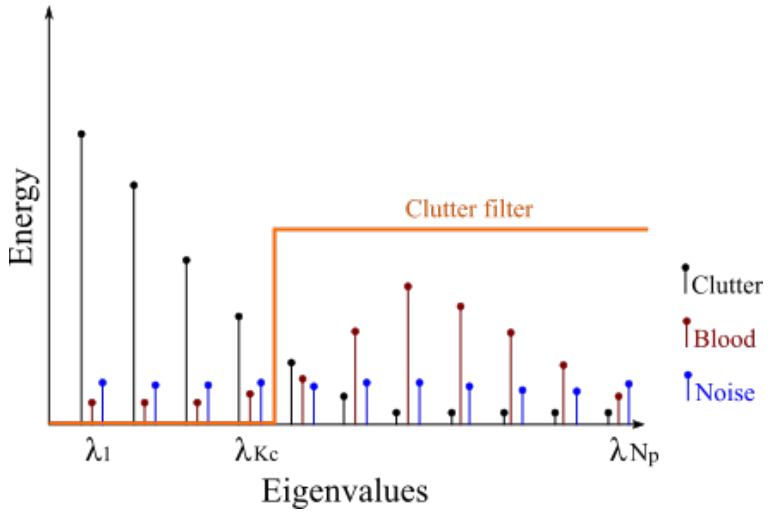


Figure 2.1: Illustration of the concept for the eigenvalue regression filter. All eigenvalues $\lambda$ contain the power represented by clutter, blood and noise, but clutter and blood dominate for different eigenvalues.

tained in separate eigenvectors. Every eigenvector will have some contribution from both clutter, blood and noise signal. If the tissue and blood signals are sufficiently uncorrelated, different eigenvectors will contain mostly clutter, or blood signal. When the clutter and blood signals are correlated then the same eigenvectors will contain comparable signal strength for both clutter and blood signal making filtering difficult. The correlation between the clutter and blood signals decreases by increasing the packet size, and also for increasing difference on blood and clutter velocity, Ledoux et al. (1997). In the ideal case, with stationary clutter, there should be perfect correlation and all clutter signals would be contained in one eigenvector. Noise is assumed to have constant eigenvalues and are contained in all eigenvectors.

Some of the proposed methods to select the clutter subspace was mentioned in the introduction, section 1.1. Two of the fully automatic approaches, the AIC and the MDL, calculate the clutter subspace based on a sufficient statistic. The sufficient statistic is the ratio of the arithmetic mean to the geometric mean of the eigenvalues $\lambda_i$ of the blood subspace, as

$$\delta_k(\lambda) = \left(\frac{1}{N_p-k}\sum_{i=k+1}^{N_p}\lambda_i\right)\Bigg/\left(\prod_{i=k+1}^{N_p}\lambda_i\right)^{\frac{1}{N_p-k}} \tag{2.9}$$

Where $N_p$ is the packet size and $\lambda_k$ is the last eigenvalue in the clutter subspace, Wax and Kailath

(1985).

The AIC is formulated as

$$\mathrm{AIC}(k) = -2N_p(N_p-k)\log\delta_k(\lambda) + 2k(2N_p-k) \tag{2.10}$$

and the MDL is formulated as

$$\mathrm{MDL}(k) = -2N_p(N_p-k)\log\delta_k(\lambda) + \frac{1}{2}k(2M-k)\log(N_p) \tag{2.11}$$

where $\delta_k$ is the sufficient statistic. This has to be calculated for each possible value $k$ of $K_c$, and the value $k$ that minimizes the AIC or MDL determine the clutter subspace $K_c$, Wax and Kailath (1985), Allam et al. (1996).

## 2.4 Nyquist Limit

To avoid aliasing in color flow imaging the $PRF$ should be equal or higher than the highest Doppler shift, $PRF > 2f_d$. This is the Nyquist limit in pulsed wave Doppler. To get sufficient axial resolution the $PRF$ is also limited by the two-way-distanse $PRF < c/2z$. These two constraints together with the equation for the mean Doppler shift $f_d = 2f_0 v/c$ give an expression for the maximum detectable velocity along the beam axis

$$v_{\mathrm{Nyquist}} = \frac{c \cdot PRF}{4f_0}, \tag{2.12}$$

and this velocity is called the Nyquist velocity in pulsed wave Doppler.

## 2.5 Image Artefacts in Color Flow Imaging

Image artefacts are distortions in the image that look like real structures. The speckle pattern in ultrasound images is an example of an image artefact. It originate from the diffraction pattern from scatterers smaller than $\lambda/2$, like blood and tissue cells. For velocities higher than the Nyquist velocity aliasing will distort the image, and this is another type of image artefact in color

flow images. The color flow will, in this case typically show negative velocities in a region with positive velocities because the Doppler spectrum wraps around itself. From equation 2.12 there is always an upper limit for the axial velocity measurement, so this image artefact is difficult to avoid. In color flow images color blooming occurs because the resolution of the color flow image is lower than the B-mode image, and the color seem to leak into the tissue. If the clutter signal attenuation is not sufficient, then flash artefacts will show in the color flow image. This is typically seen as flashes of colour in areas without blood.

## 2.6 Multi-Dimensional Blood Velocity Estimation

Vortex visualization might be used as an aid when diagnosing heart diseases. The vortex formation in the blood flow forming in the end of the distole and beginning of the systole is of particular interest, Gharib et al. (2006). In ultrasound Doppler only the axial blood velocity is estimated, while this vortex is a three dimensional complex pattern. In regular color flow imaging it is not possible to visualize the full three dimensional velocity vector, since the estimated velocity is angle-dependent.

Multi-dimensional blood velocity estimation methods have been proposed to facilitate visualization of the blood flow. The two main research fields for multi-dimensional blood flow velocity estimation are vector Doppler and speckle tracking. In vector Doppler triangularization is used to estimate the lateral velocity component, and ultrasound beams are transmitted and received from different angles Dunmire et al. (2000).

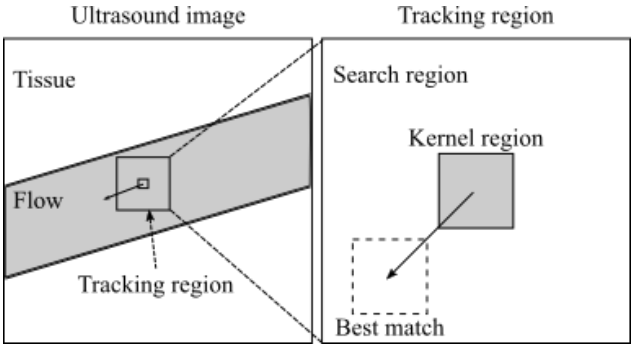


Figure 2.2: Illustration of the speckle tracking concept. The best match for the 2D image kernel in the next frame is used to estimate the velocity.

In speckle tracking, pattern matching techniques are used to track the blood speckle in the

ultrasound image between frames. An image kernel is defined, and the best match of the kernel in the subsequent frame is used together with the $PRF$ to calculate the movement of the kernel. The velocity is estimated for all imaging points and are visualized as arrows in a vector velocity map Bohs et al. (2000) Trahey et al. (1987). Figure 2.2 is an illustration of the speckle tracking concept.

Pattern matching algorithms used for the speckle tracking operate on the radio-frequency (RF) signals like the normalized cross-correlation or on the extracted envelope of the signal, like the sum of absolute differences (SAD), and sum of squared differences (SSD). The two latter are less computer intensive, Bohs et al. (2000).

### 2.6.1 Normalized Cross-Correlation

The most likely displacement of the kernel $K$ for the normalized cross-correlation algorithm, is given by the index of the maximum correlation value, according to

$$\rho(u,v) = \frac{\sum_{x,y}(I(x+u,y+v) - \bar{I}_{u,v})(K(x,y) - \bar{K})}{\sqrt{\sum_{x,y}(I(x+u,y+v) - \bar{I}_{u,v})^2 \sum_{x,y}(K(x,y) - \bar{K})^2}}, \tag{2.13}$$

where $I$ is the search region displaced $(u,v)$ from the kernel position for a subsequent frame. The average of the search region and the kernel is defined by

$$\bar{I}_{u,v} = \frac{1}{N_x N_y}\sum_{x,y} I(x+u,y+v), \quad \bar{K} = \frac{1}{N_x N_y}\sum_{x,y} K(x,y), \tag{2.14}$$

where $N_x$ and $N_y$ are the kernel dimensions.

### 2.6.2 Sum of Absolute Differences (SAD), and Sum of Squared Differences (SSD)

For the SAD, and the SSD algorithm a coefficient representing the error for the match is calculated according to

$$d_{SAD}(u,v) = \sum_{x,y} |I(x+u,y+v) - K(x,y)|, \tag{2.15}$$

$$d_{SSD}(u,v) = \sum_{x,y}(I(x+u, y+v) - K(x,y))^2, \tag{2.16}$$

respectively. The displacement is given by the match that yields the minimum error. $I$ is the search region, and $K$ is the kernel.

## 2.7 Tissue Spectral Doppler

Tissue spectral Doppler shows the spectral content of the Doppler frequencies for a given region, and how it changes in time. It is a grayscale image of the periodogram in two dimensions where the brightness of each pixel indicates the count of that Doppler frequency. Most often, the time is represented along the horizontal axis and velocities, calculated from equation 2.2, are displayed on the vertical axis, instead of the Doppler frequency. The tissue spectral Doppler image is often termed the sonogram.

For a continous aquisition, the resolution of the sonogram can be improved by applying the sliding window fast fourier transform (FFT). Instead of using fixed bins, the bins overlap by 50 % and is windowed, Manolakis and Ingle (2011).

# Chapter 3

# Methods

## 3.1 Data Aquisition

### 3.1.1 *In Vivo* Data

A total of nine *in vivo* datasets were used in this project. Two datasets (*Testdata1* and *Testdata2*) were recorded using a research scanner, Verasonics Vantage system (Verasonics, Inc., USA). Both were apical views of the left ventricle from the same healthy volunteer, with different $PRF$. A continuous acquisition with diverging waves insonifying the whole field-of-view was used and RF channel data was stored for further processing. Dataset *Testdata1* had $PRF$ of 2000 Hz and dataset *Testdata2* had $PRF$ of 4000 Hz. In addition, previously recorded datasets from patients were used, and those had been recorded with a GE Vivid E9 scanner using research software developed by GE Vingmed, Horten, Norway. *Patient1* refers to a recording of an apical view of the left ventricle from a child suffering from a side effect of cancer treatment, more specifically antracyclin induced dilated cardiomyopathy. The child was seven years old, and weighed 20 kg. *Control1* refers to a recording of an apical view of the left ventricle from a healthy child. The child was six years old and weighed 23 kg. These four datasets were analyzed more in depth, and the remaining datasets was used to evaluate the clutter subspace selection methods. Table 3.1 gives an overview of the data, including information on the heart rate in beats per minute ($BPM$), the $PRF$, the center frequency $f_0$, the packet size, the probe and the scanner.

| Dataset | Healthy | Heartrate [BPM] | *PRF* [kHz] | $f_0$ [MHz] | $N_p$ | Probe | Scanner |
|---|---|---|---|---|---|---|---|
| Testdata1 | Yes | | 2 | 2.9 | Continous | Phased | Verasonics |
| Testdata2 | Yes | | 4 | 2.9 | Continous | Phased | Verasonics |
| Control1 | Yes | 73 | 5 | 3.7 | 16 | 6S Phased | GE Vivid E9 |
| Control2 | Yes | 109 | 7 | 5.8 | 16 | 12S Phased | GE Vivid E9 |
| Control3 | Yes | 109 | 7 | 5.8 | 16 | 12S Phased | GE Vivid E9 |
| Patient1 | No | 127 | 5 | 3.7 | 16 | 6S Phased | GE Vivid E9 |
| Patient2 | No | 107 | 8 | 5 | 16 | 9L Linear | GE Vivid E9 |
| Patient3 | No | 157 | 5 | 4.5 | 16 | 9L Linear | GE Vivid E9 |
| Patient4 | No | 162 | 5 | 4.5 | 16 | 9L Linear | GE Vivid E9 |

Table 3.1: *in vivo* data and meta data

### 3.1.2 Simulations

In order to evaluate the performance of the eigenvalue regression filter a total of seven simulations were carried out using the Field II simulation software, Jensen (1996). Channel RF data was simulated for a linear scan, and both clutter and blood signal were simulated as plug flow with constant velocity in a cylindrical phantom. The Doppler angle of the phantom was 60 deg. The number of blood scatterers per resolution cell was 10. Random noise was added to the signals, and the $SNR$ was 40 dB. For *Simulation1* there was only one velocity present in the phantom and the absolute velocity was 0.1 m/s representing clutter movement. For *Simulation2*, *Simulation3*, *Simulation4* and *Simulation5* there was one plug flow with absolute velocity 0.1 m/s representing clutter movement, and one plug flow representing blood movement. The different blood velocities were 0.15 m/s for *Simulation2*, 0.2 m/s for *Simulation3*, 0.25 m/s for *Simulation4* and 0.3 m/s for *Simulation5*. The $SCR$ for the simulations was $-25$ dB. These simulations were used to determine how the eigenvalues were distributed in the case of low velocity difference, and high velocity difference between clutter and blood signals. In *Simulation6* and *Simulation7* the absolute velocity of the phantom representing clutter and blood was chosen as the maximum absolute velocity found *in vivo* data *Testdata2* for a frame in systole and a frame in diastole. This was found by inspection of the sonogram. *Simulation6* and *Simulation7* was used to calculate the bias of the velocity estimates from speckle tracking and evaluate the performance of the eigenvalue regression filter compared to polynomial regression filter and the FIR filter. For all the simulations the $PRF$ was 4 kHz, center frequency $f_0$ was 5 kHz. The parameters used for the

| Dataset | Blood phantom velocity [m/s] | Clutter phantom velocity [m/s] | $PRF$ [kHz] | $f_0$ [MHz] | Packet size | Scan |
|---|---|---|---|---|---|---|
| Simulation1 | | 0.1 | 4 | 5 | Continous | Linear |
| Simulation2 | 0.15 | 0.1 | 4 | 5 | Continous | Linear |
| Simulation3 | 0.2 | 0.1 | 4 | 5 | Continous | Linear |
| Simulation4 | 0.25 | 0.1 | 4 | 5 | Continous | Linear |
| Simulation5 | 0.3 | 0.1 | 4 | 5 | Continous | Linear |
| Simulation6 | 0.5 | 0.15 | 4 | 5 | Continous | Linear |
| Simulation7 | 0.15 | 0.03 | 4 | 5 | Continous | Linear |

Table 3.2: Simulation parameters

simulations are listed in table 3.2.

## 3.2 Post Processing of Data

The datasets from the Verasonics scanner were stored as channel data and beamformed off-line. The signal envelope was extracted using complex demodulation. Dynamic receive focusing was used to get higher signal intensity and higher lateral resolution. Focusing on receive is obtained by multiplying with a phase factor. The phase is calculated for each time sample according to the two-way distance $z = c_0 t/2$.

The patient and control datasets recorded with the GE Vivid E9 scanner were scan converted. Interpolation was used to convert the data from cartesian to polar coordinates.

## 3.3 Sonogram and Frequency Spectrum

The improved Sonogram using the sliding window FFT was calculated for *Testdata1* and *Testdata2* as described in section 2.7. The sonogram for *Testdata2* was used to find the maximum absolute velocity for a frame in systole and diastole. To verify that the velocity was in the axial direction, the blood flow was displayed in a video of B-mode images. The spectral content was calculated for three different spatial points and five different temporal points for *Testdata2*. This was used together with B-mode and color flow images of the dataset to evaluate the performance of the FIR-filter and to verify the need for an adaptive clutter filter.

## 3.4 Eigenvalue Regression Filter as Adaptive Filter

The eigenvalue regression filter was implemented using a multi-ensemble-based formulation, Yu and Løvstakken (2010). The eigenvalue regression filter is a two-dimensional filter. Since the correlation matrix of the blood, clutter and noise signals is calculated for each frame, and is used in calculating the filter basis as explained in section 2.3, the eigenvalue regression filter adapt to tissue motion in time. The clutter subspace varies for each frame, and there is, therefore, the possibility to also set the size of the clutter subspace for each frame adaptivily to achieve optimum clutter rejection, Yu and Løvstakken (2010). Since the eigenvalues represent the signal strength of the eigenvector, the power of each eigenvalue was calculated and the eigenvalues above a power threshold value was considered the clutter subspace.

Some previously purposed methods to select the clutter subspace was mentioned in the introduction, and an overview of some of these methods are given below.

- **Minimax**, guarantee quantitatively accurate recovery of a signal matrix $c$ from a signal matrix $s = c + n$ containing noise $n$ by applying soft thresholding to the singular values of $s$, Donoho and Gavish (2014). This is not directly applicable for setting a blood threshold value since the blood signal is not standard gaussian noise, and noise signal will also be present.

- **Robust Principal Component Analysis (PCA)**, for a signal matrix $s = c + b$ consisting of a low rank matrix $c$ and a sparse matrix $b$. When the sparse matrix $b$ is a small perturbation of the signal matrix $s$, it is possible to disentangle the low-rank and sparse components exactly by convex programming. It is not known how well the rank of $c$ and $b$ would be estimated if the sparse matrix was dense instead. In that case the signal $b$ could be considered a sum of a sparse and a dense matrix, Candès et al. (2005). For *in vivo* data the blood signal is considered a small perturbation of the signal matrix since the power of the clutter signal is much higher than the blood signal. Demené et al. (2015) suggest that blood signal can be considered a sparse matrix. For a simulation where the blood signal is only present for a particular region like in a blood phantom, then the blood signal would be sparse. For *in vivo* data some blood signal is present in all image pixels and it is unknown whether the blood signal can be considered a sparse matrix.

- **Akaike information criterion**, using the Akaike information criterion (AIC) or the Minimum description length (MDL) to determine the size of the clutter subspace, when a sufficient statistic is assumed to be the ratio of the arithmetic mean to the geometric mean of the eigenvalues of the covariance matrix, Allam et al. (1996) Wax and Kailath (1985).

- **Dynamic mean evaluation**, to find the first eigenvalue corresponding to noise all possible sizes of the clutter subspace are considered, in an efficient way, and a if test is performed to decide the order. If the distance to the first eigenvalue (clutter) is the shortest it is considered a part of the clutter subspace, or if the distance to the last eigenvalue (noise) is the shortest it is part of the noise subspace. When calculating the distance the signal is modeled using AR polynomial representation, Fort et al. (1995). This is also not directly applicable for setting a blood threshold, but might be if noise is properly removed first.

In this work the power threshold for the *in vivo* data was chosen for each frame. Three different methods were considered. One semi-automatic method where the power threshold was set equal to the difference in decibels between a clutter ROI and a blood ROI. The blood ROI was assumed to contain signals from blood, clutter and noise, and the clutter ROI was assumed to contain signals from clutter and noise. The difference should yield the power of the blood signal, and this method is similar to one of the methods purposed by Demené et al. (2015). Two other fully automatic methods for selecting the clutter subspace was also tested. These two methods was the AIC and the MDL, as mentioned above, and explained in the end of section 2.3. The subspace selected using these methods were compared to the clutter subspace chosen manually. For the simulations, the power threshold was set equal the $SCR$.

Since blood velocities are normally larger than clutter velocities it is also possible to set a velocity threshold to select clutter subspace. This can be done by calculating the Doppler velocity of each eigenvector. This was used when filtering the simulated data as the clutter velocity in the simulation was known, and could easily be set as the velocity threshold value. Setting a Doppler velocity threshold for the *in vivo* data was not looked further into. The underestimation of the true clutter velocity was a problem for the case where all beam and range samples were used as the ROI.

## 3.5 Visualization of the Eigenvectors

In order to manually select the clutter subspace, the projection of each eigenvector onto the data from the selected frame was displayed as its own B-mode image, resulting in as many B-mode images as the size of the packet. To better visualize where in the image the signal representing clutter, blood and noise originated, all these B-mode images were given a color and superimposed using the quadratic mean of the *RGB*-value into one image. The B-mode images of each eigenvector for a frame in diastole for dataset *Testdata2* are shown in figure 4.11, and the result of the superimposed image of the same frame is shown in figure 4.10a, and these results are presented in section 4.2.

The spectral content of each eigenvector was calculated using the sliding window FFT, and the frequency was converted to yield Doppler velocity. The distribution of energy in decibels of the spectral content for each eigenvector was displayed in an image as a colormap. Images was generated for *Simulation1*, *Simulation2*, and *Simulation5*, and for *in vivo* data *Testdata1*. This was done for one frame in systole, and one frame in diastole, for packet size sixteen, sixty four and for a packet consisting of all temporal samples. The images from the three simulations were used to determine the effect of the difference in velocity, between clutter and blood signals, on the spectral content of the eigenvectors. The images from the *in vivo* data were used to determine the effect of increasing packet size on the spectral content of the eigenvectors.

## 3.6 Speckle Tracking

Speckle tracking was used to aquire velocity estimates of the blood flow in *Simulation6* and *Simulation7*. These simulations were filtered with the eigenvalue regression filter and the FIR filter, and the bias were calculated for the two cases for each simulation. Speckle tracking was also used to visualize the vortex formation of blood in the left ventricle during diastole for the test data with the highest PRF, *Testdata2*, and the patient data *Patient1*, *Control1*. The width of the phantom was 1 cm and the diameter was 3 cm. And, for the speckle tracking of the simulation data, a spatial averaging region of 3.8 mm in the axial direction and 3.3 mm in the lateral direction was used. The width of the left ventricle in *in vivo* data *Testdata2* was approximately 10 cm and the length was approximately 15 cm. And, for the speckle tracking a spatial averaging re-

gion of 12 mm in the axial direction and 13 mm in the lateral direction was used. The width of the left ventricle in *in vivo* data *Patient1* and *Control1* was approximately 5 cm and the length was approximately 6 cm. For *Patient1* and *Control1* a spatial averaging region of 7 mm in the axial direction and 7 mm in the lateral direction was used. A temporal averaging of 40 ms was used for all.

# Chapter 4

# Results

## 4.1 Presentation of Dataset *Testdata1* and *Testdata2*

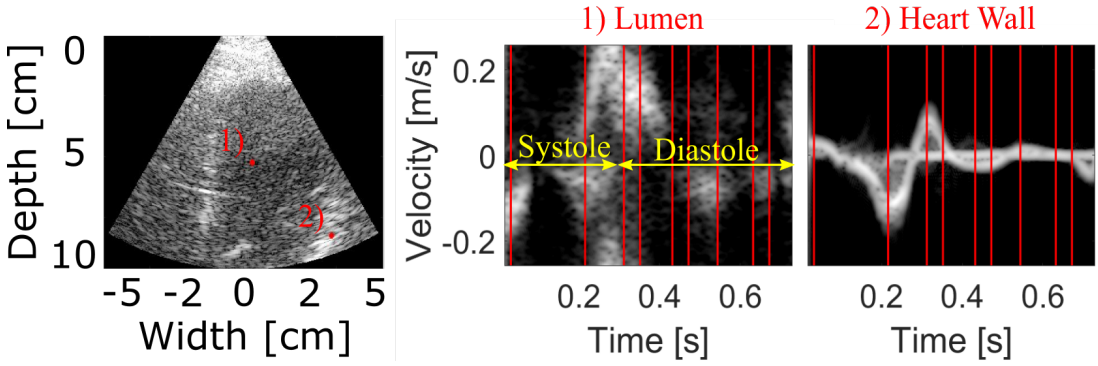


Figure 4.1: Sonogram for dataset *Testdata1* for the regions marked in the left figure displaying the B-mode image. The ROIs are 26 mm in depth and 0.83 mm in width. Yellow arrows indicate the systole and diastole. Two frames in systole and seven frames in diastole are indicated with red lines and are displayed as B-mode and color flow images in figure 4.3 and 4.4 respectively.

In order to develop and test the eigenvalue regression filter, datasets *Testdata1* and *Testdata2* were analyzed in different ways as stated in section 1.4. These two datasets are presented below.

Figure 4.1 shows the sonogram for *in vivo* data *Testdata1* for a region in the heart wall and a region in the lumen. Yellow arrows indicate systole and diastole and two frames in systole and seven frames in diastole are indicated with red lines. These frames was filtered with the FIR filter and displayed as B-mode images in figure 4.3, and color flow images in figure 4.4. Similarly for dataset *Testdata2*, the frames marked with red lines in figure 4.2 are displayed as B-mode images in figure 4.5, and color flow images in figure 4.6. These figures also indicate the systole

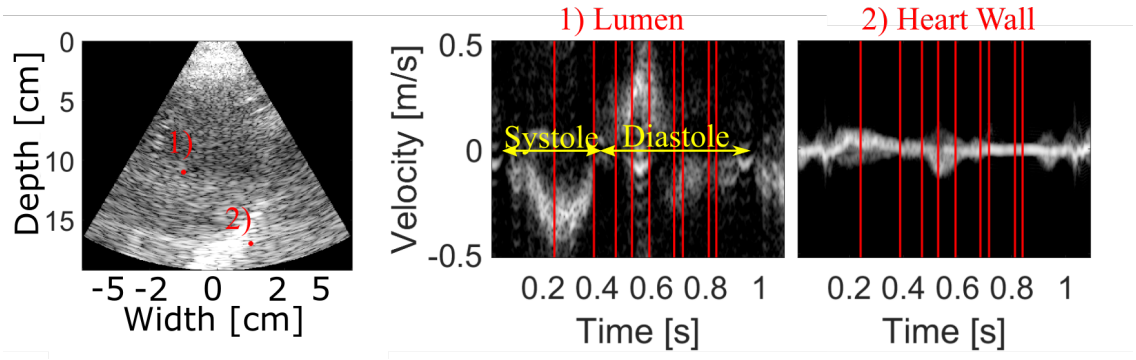


Figure 4.2: Sonogram for dataset *Testdata2* for the regions marked in the left figure displaying the B-mode image. The ROIs are 26 mm in depth and 0.83 mm in width. Yellow arrows indicate the systole and diastole. Two frames in systole and seven frames in diastole are indicated with red lines and are displayed as B-mode and color flow images in figure 4.5 and 4.6 respectively.

and diastole with red arrows. Both datasets were apical views showing the left ventricle. In both cases the first two frames show outflow of blood from the left ventricle through the aortic valve. The aortic valve is not visible in this view. The next frames show inflow of blood through the mitral valve. In the B-mode images, the mitral valve is visible in the bottow center of the frame at $t = 0.312$ s for dataset *Testdata1*, and $t = 0.684$ s for dataset *Testdata2*. The opening of the mitral valve indicate the beginning of diastole, and in the subsequent frames there is possible vortex formation in the blood flow. The $PRF$, center frequency $f_0$, and information on the probe and scanner used for the recording of these two datasets can be found in table 3.1.

## 4.2 Investigate the Potential of Adaptive Eigenvalue Regression Filter in Cardiac Imaging

Figure 4.7 shows the frequency spectrum for different spatial points for five frames in diastole for dataset *Testdata2*. At time points $t = 0.4680$ s, and $t = 0.5920$ s, the frequency spectrum of the spatial point in the tissue region close to the mitral valve (right) and the spatial point in the lumen (middle) are comparable in strength. This shows that the attenuation of the FIR-filter within the stopband is too low. The signal power for both spatial points are around 50 dB, and by looking at the B-mode image in figure 4.5 this is visible as tissue flashing for depth 10 cm. At $t = 0.5279$ s the spatial point in the tissue region close to the mitral valve (right) shows that the

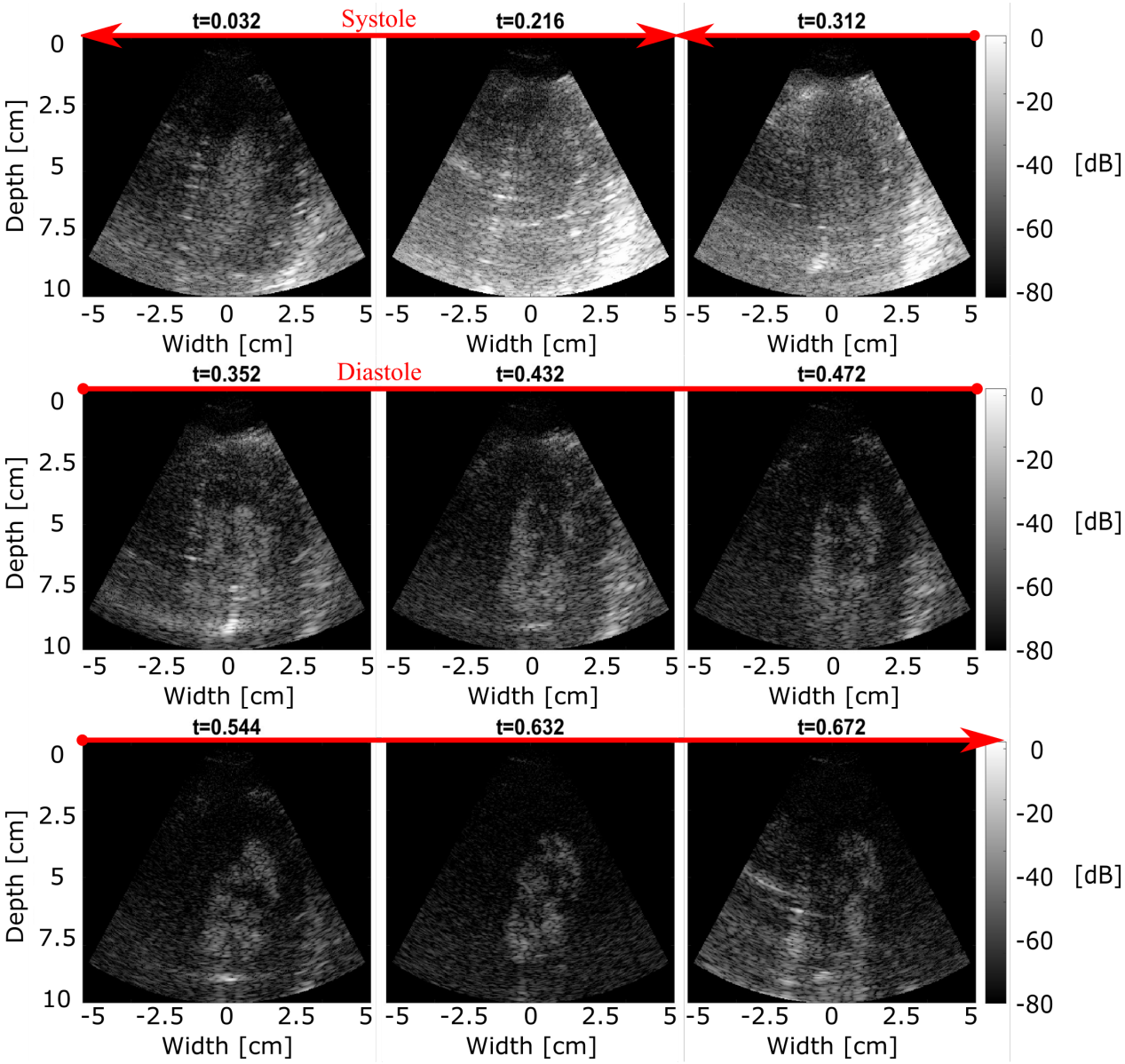


Figure 4.3: B-mode images of the filtered dataset *Testdata1* using the FIR-filter at different times during the heart cycle. Red arrows indicate the systole and diastole.

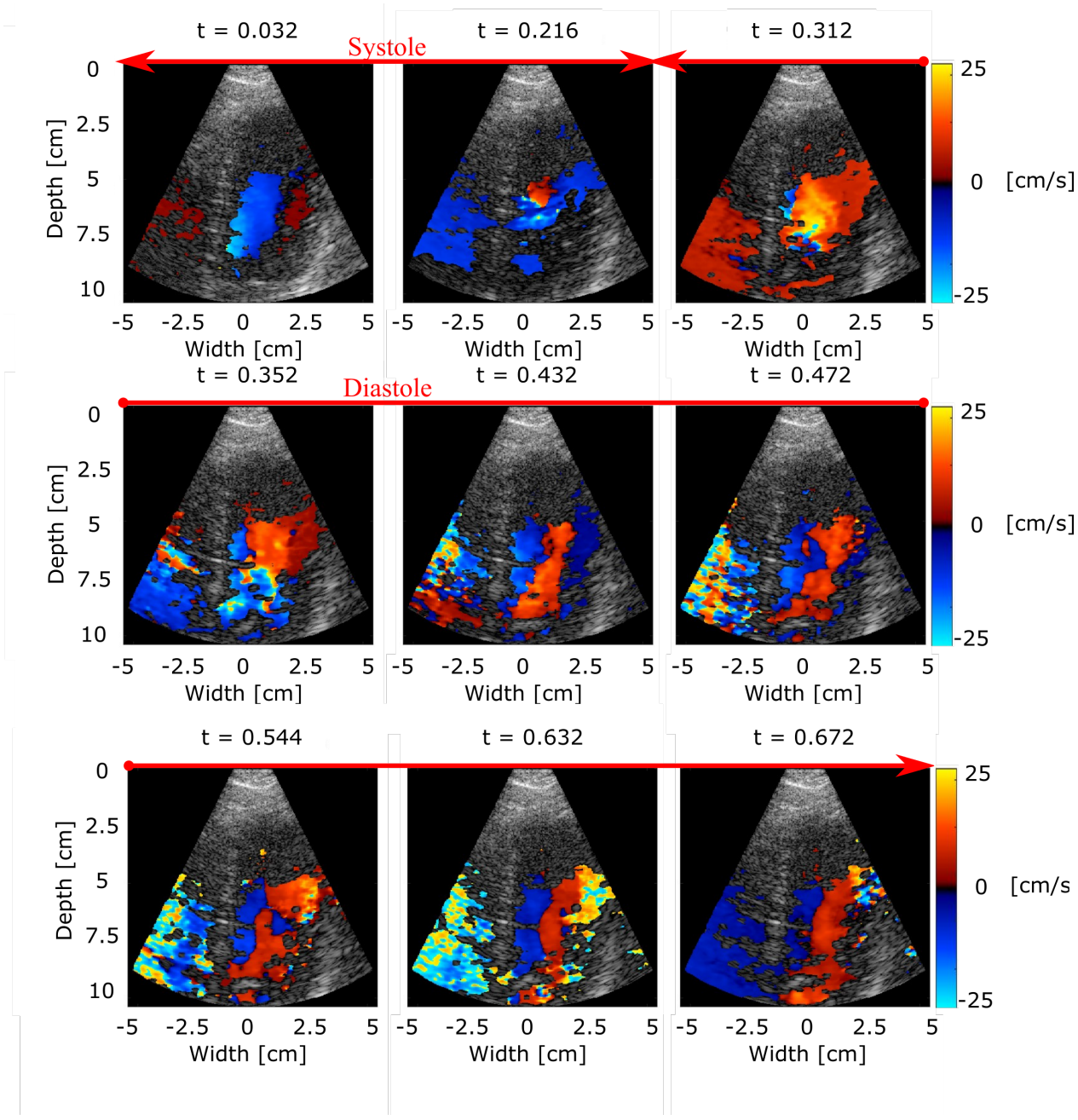


Figure 4.4: Color flow images of the filtered dataset *Testdata1* using the FIR-filter at different times during the heart cycle. Red arrows indicate the systole and diastole.

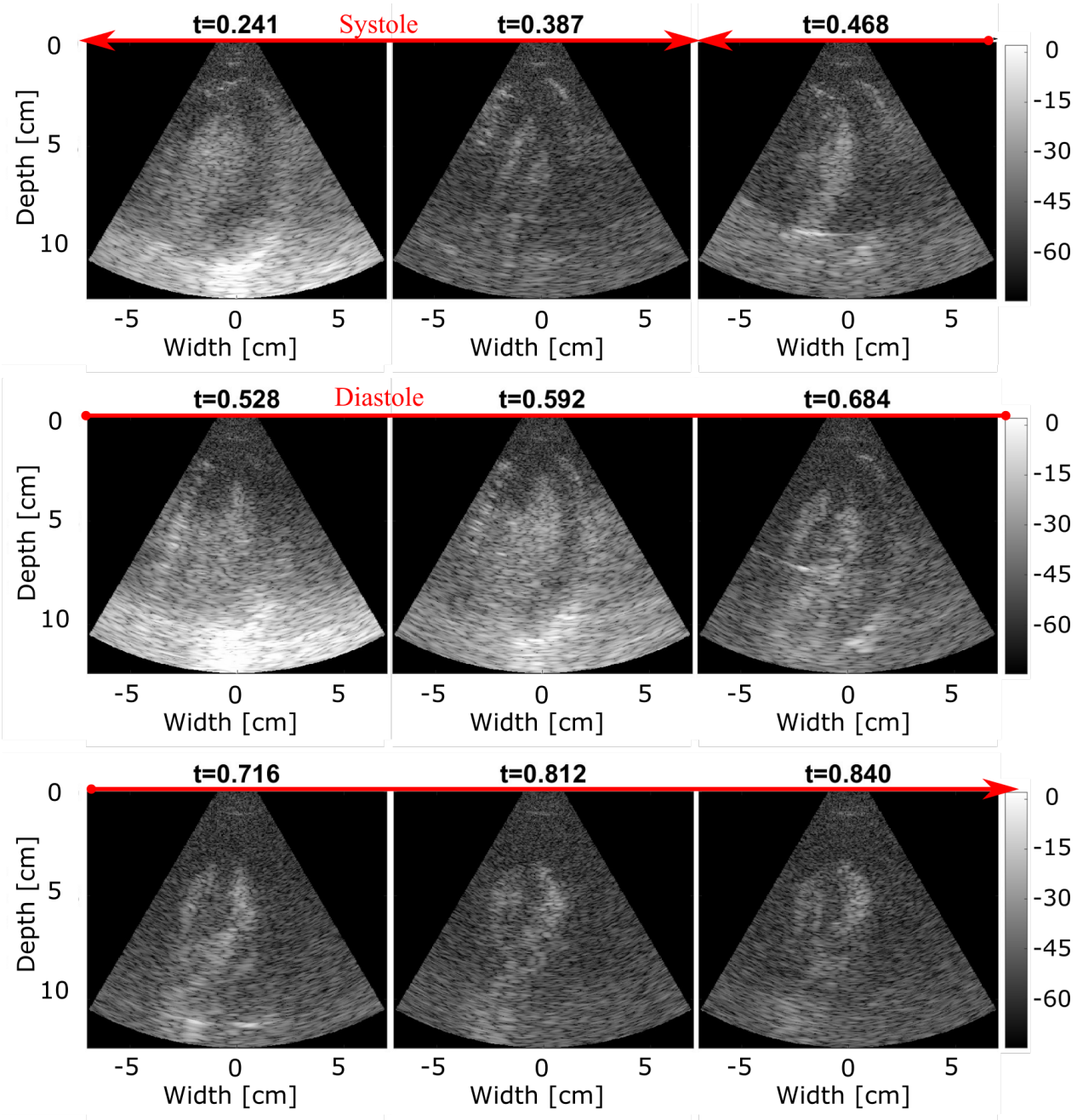


Figure 4.5: B-mode images of the filtered dataset *Testdata2* using the FIR-filter at different times during the heart cycle. Red arrows indicate the systole and diastole.

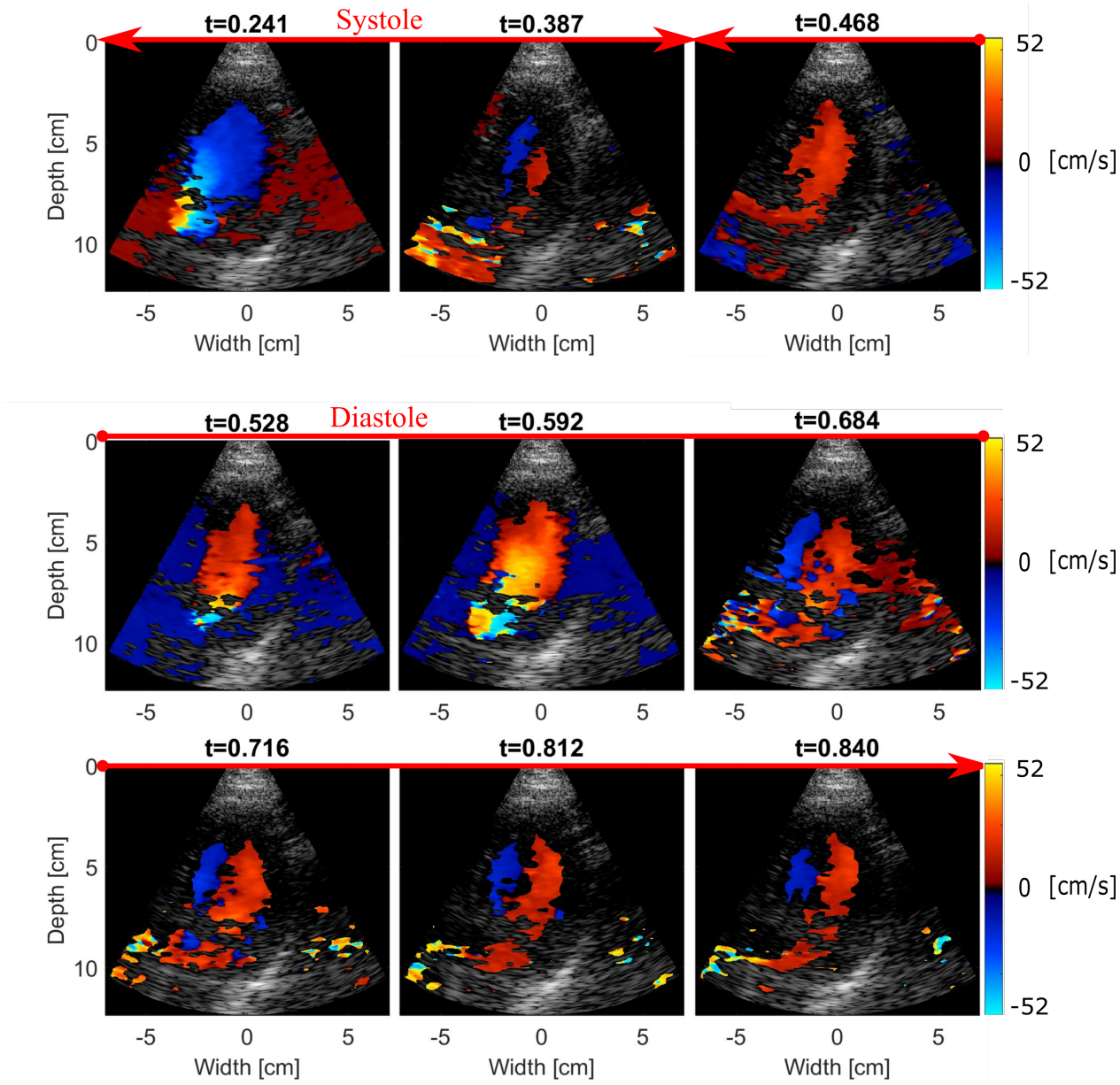


Figure 4.6: Color flow images of the filtered dataset *Testdata2* using the FIR-filter at different times during the heart cycle. Red arrows indicate the systole and diastole.

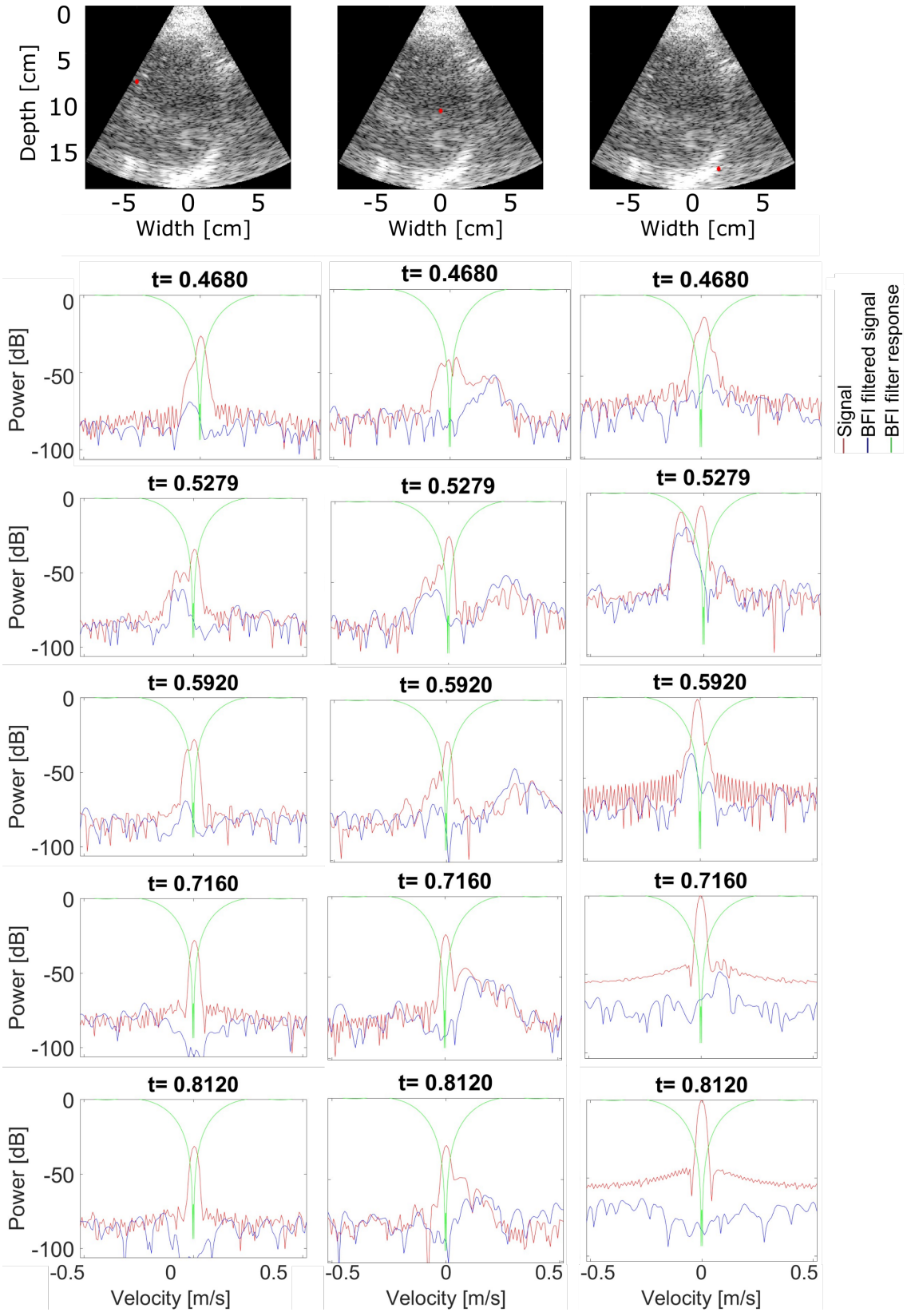


Figure 4.7: Signal, signal filtered using the FIR filter, and the FIR filter response from dataset *Testdata2* in the lumen, in the heart wall and in the ventricular septum at different times during the diastole. The ROI is one beam sample and ten range samples with center indicated in the B-mode images in the top row as a red mark.

tissue signal falls within the passband of the FIR-filter. From the B-mode image this tissue signal is hiding the blood signal which is only barely visible at depth 5 cm. By looking at the frequency spectrum at time points $t = 0.7160$ s and $t = 0.8120$ s the long transition region of the FIR-filter causes some blood drop out as the blood signal is also attenuated by the FIR-filter. The blood drop-out is visible in the B-mode image as a region with lower intensity in the middle of the blood signal at depth 5 cm.

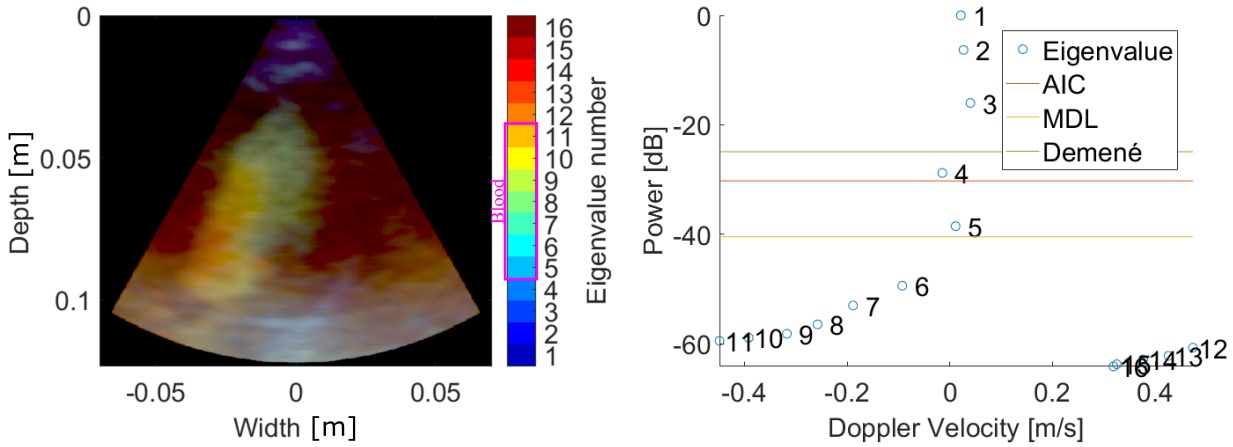


(a) Eigenvectors projected onto data subspace and shown with different colors for dataset *Testdata2* at time point $t$ =0.241 s in systole. The pink box indicates which eigenvectors represent blood signal the most.

(b) Corresponding eigenvalues for dataset *Testdata2* at time point $t$ =0.241 s in systole. The adaptive power thresholds for this frame are indicated as horizontal lines.

Figure 4.8: Eigenvectors and eigenvalues for *Testdata2* at time point $t$ =0.241 s with outflow in systole. For this frame the adaptive power threshold is in agreement with the eigenvectors representing blood signal selected manually.

One frame in systole and two in diastole for *in vivo* data *Testdata2*, was filtered as explained in section 3.5. The frame in systole was at time point $t = 0.241$ s with outflow, one frame in diastole was at time point 0.5920 s with inflow, and the other at time point 0.8129 s with vortex formation. The frame in systole with outflow is shown in figure 4.8a, the frame in diastole with inflow in figure 4.9a and the frame in diastole with vortex formation in figure 4.10a, where each eigenvector corresponds to a colour. The pink box indicates which eigenvectors correspond to the blood signal. This was decided by looking at the image of each individual eigenvector which is shown in figure 4.11 for the frame in diastole. The eigenvalues for the frame in systole and the two frames in diastole are shown in figures 4.8b, 4.9b and 4.10b. The adaptive power threshold

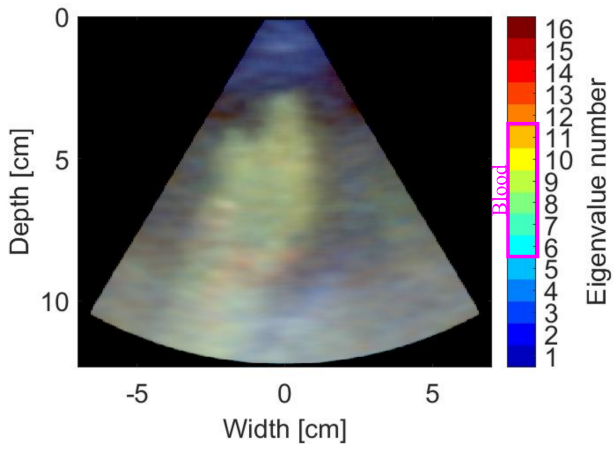


(a) Eigenvectors projected onto data subspace and shown with different colors for dataset *Testdata2* at time point $t$ =0.5920 s in diastole. The pink box indicates which eigenvectors represent blood signal the most.

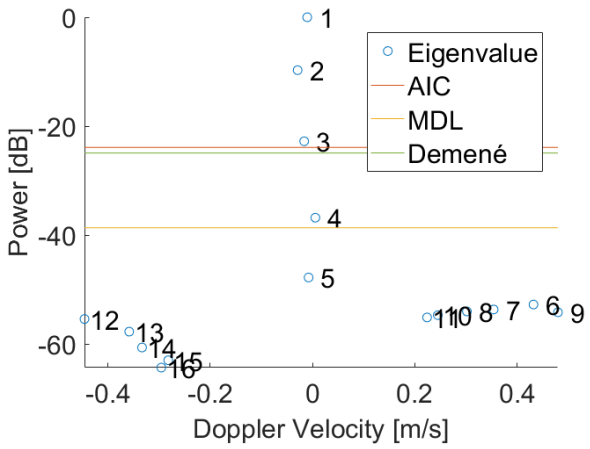


(b) Corresponding eigenvalues for dataset *Testdata2* at time point $t$ =0.5920 s in diastole. The adaptive power thresholds for this frame are indicated as horizontal lines.

Figure 4.9: Eigenvectors and eigenvalues for *Testdata2* at time point $t$ =0.5920 s with inflow in diastole. In this frame the adaptive power threshold was too high, and not in agreement with the eigenvectors representing blood signal selected manually.

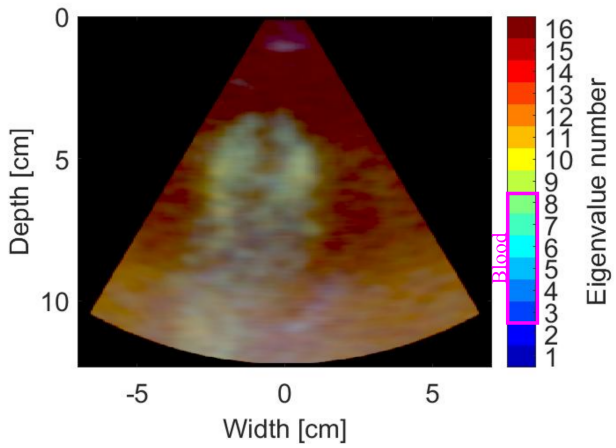


(a) Eigenvectors projected onto data subspace and shown with different colors for dataset *Testdata2* at time point $t$ =0.8120 s in diastole. The pink box indicates which eigenvectors represent blood signal the most.

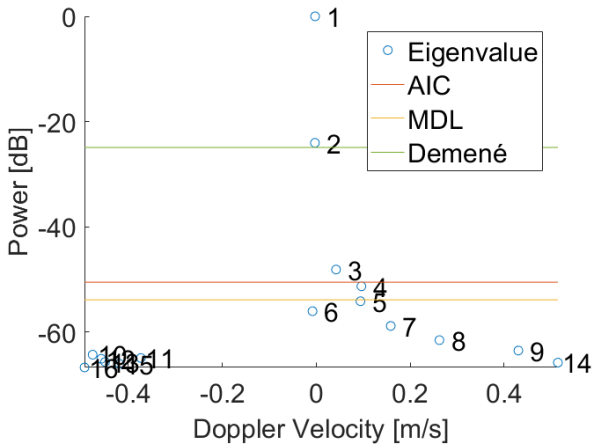


(b) Corresponding eigenvalues for dataset *Testdata2* at time point $t$ =0.8120 s in diastole. The adaptive power thresholds for this frame are indicated as horizontal lines.

Figure 4.10: Eigenvectors and eigenvalues for *Testdata2* at time point $t$ =0.8120 s with vortex formation in diastole. For this frame the adaptive power threshold is in agreement with the eigenvectors representing blood signal selected manually.

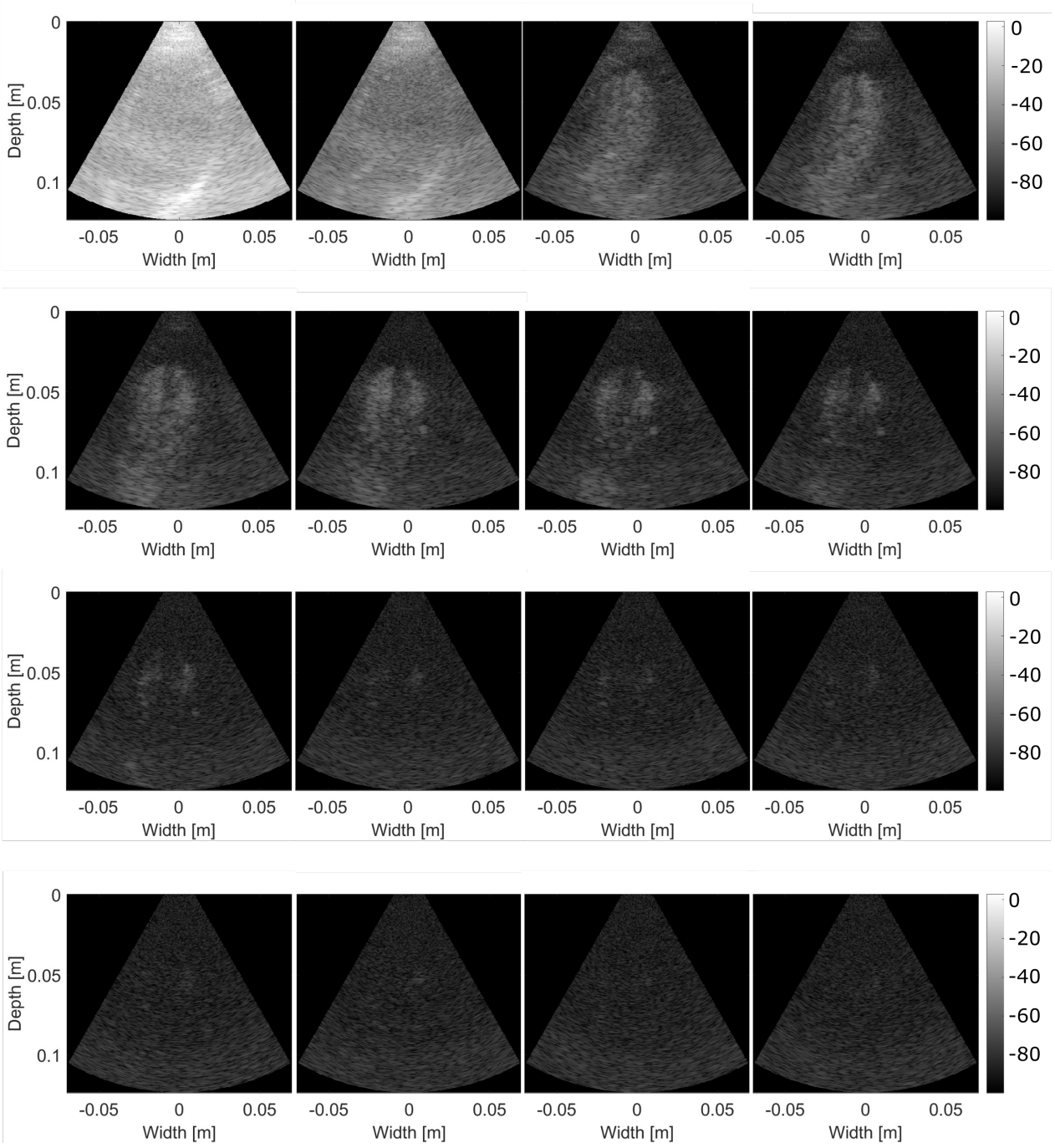


Figure 4.11: B-mode images of the projection of each eigenvector onto the data subspace for dataset *Testdata2* at time point $t$ =0.8120 s in diastole with vortex formation. Increasing eigenvector number from left to right top to bottom. The tissue signal is represented by eigenvectors 1 and 2, blood signal is represented by eigenvectors 3-8, and the remaining eigenvectors 9-16 represent noise.

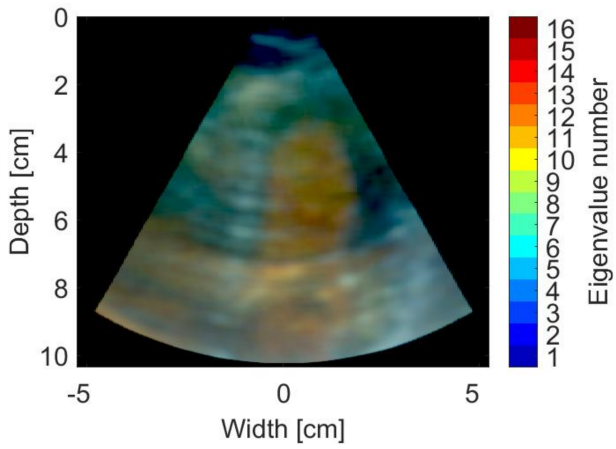


(a) Eigenvectors projected onto data subspace and shown with different colors for dataset *Testdata1* at time point $t$ =0.2160 s in systole. In this case it was not possible to distinguish between clutter, blood and noise subspace.

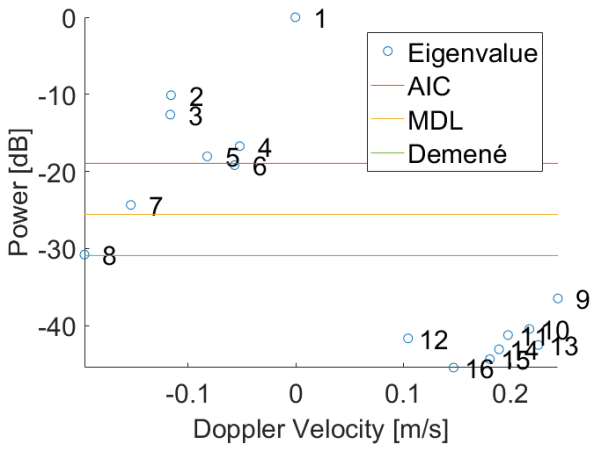


(b) Corresponding eigenvalues for dataset *Testdata1* at time point $t$ =0.2160 s in systole. The adaptive power thresholds for this frame are indicated as horizontal lines.

Figure 4.12: Eigenvectors and eigenvalues for *Testdata1* at time point $t$ =0.2160 s in systole with outflow.

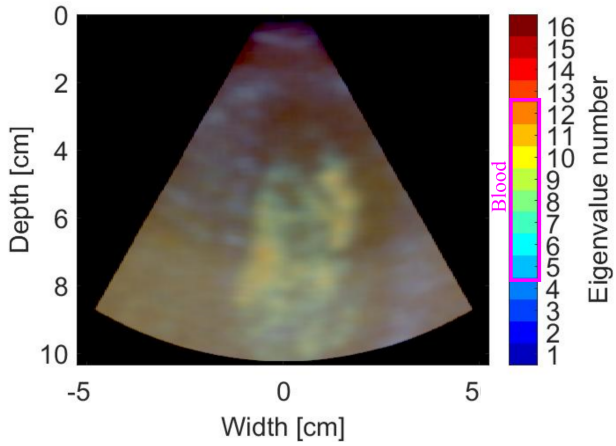


(a) Eigenvectors projected onto data subspace and shown with different colors for dataset *Testdata1* at time point $t$ =0.4720 s in diastole. The pink box indicates which eigenvectors represent blood signal the most.

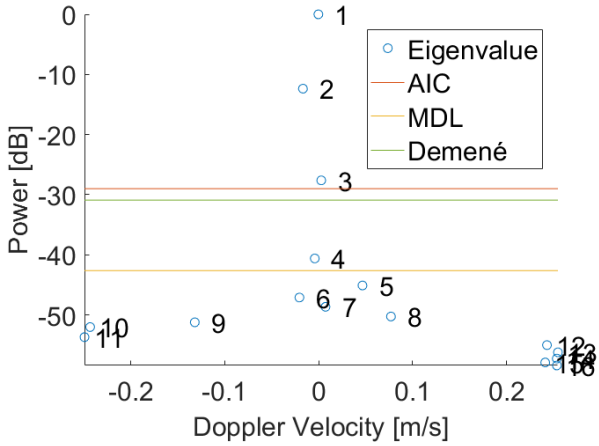


(b) Corresponding eigenvalues for dataset *Testdata1* at time point $t$ =0.4720 s in diastole with vortex formation. The adaptive power thresholds for this frame are indicated as horizontal lines.

Figure 4.13: Eigenvectors and eigenvalues for *Testdata1* at time point $t$ =0.4720 s in diastole.

was selected as explained in section 3.4 and is shown as horizontal lines.

This was also done similarily for *Testdata1*, and figure 4.12 shows the eigenvectors and eigenvalues for the frame in systole, and figure 4.13 for the frame in diastole. The frame in systole is

at time point $t = 0.216$ s and the one in diastole at $t = 0.472$ s.

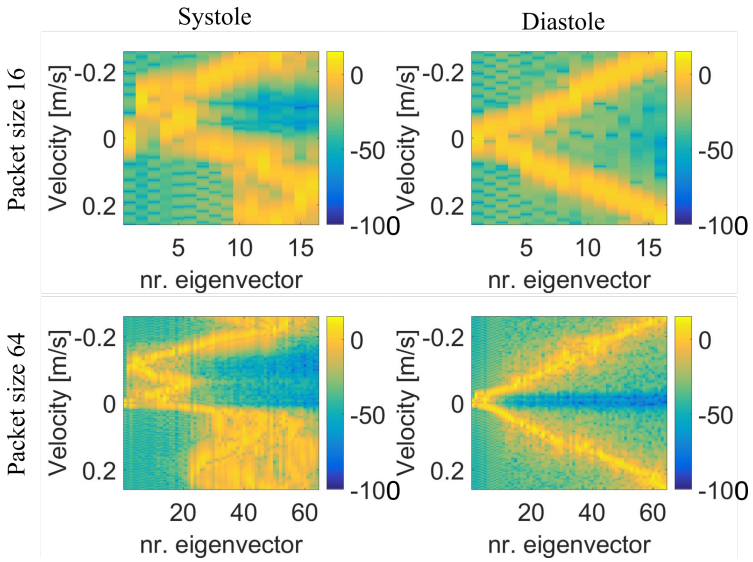


(a) Timepoint $t$ =0.2160 s in systole and $t$ =0.4720 s in diastole for packet size sixteen and sixtyfour.

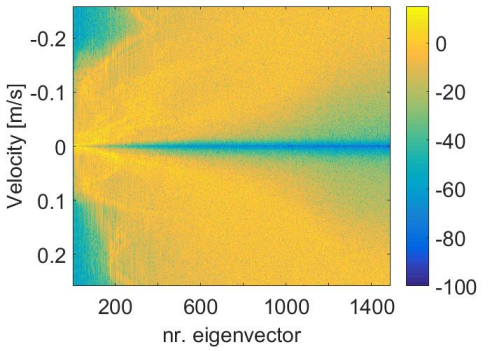


(b) Packet contain all temporal samples.

Figure 4.14: Power distribution of the spectral content of the eigenvectors as explained in section 3.5 for dataset *Testdata1* for different packet size. When one packet contains all time samples the eigenvalue regression filter becomes saturated and looses its adaptive nature. It will function as a normal highpass filter with fixed cut-off frequency.

The power distribution of the spectral content of the eigenvectors from *in vivo* data *Testdata1* are shown in figure 4.14a for packet sizes $N_p = 16$, and $N_p = 64$ for one frame in systole and one frame in diastole. Figure 4.14b shows the spectral content when the packet size consisted of all available time samples, and the packet size was $N_p = 1488$. The signals has a broader bandwidth for $N_p = 16$ than $N_p = 64$, and has the broadest bandwidth for $N_p = 1488$.

Figure 4.15 shows the effect of increasing packet size on the $SCR$. Figure 4.15a, and figure 4.15b, is from *in vivo* data *Testdata1* in systole, and diastole, respectively. The velocity and power threshold were set manually, and for the *in vivo* data the eigenvectors corresponding to blood was determined by figure 4.12a and 4.13a as eigenvectors number $11-16$ and $5-12$, respectively. The power threshold was therefore set to be $-35$ dB for systole and $-40$ dB for diastole, and the velocity threshold set to be 0.1 m/s for systole and 0.05 m/s for diastole. The $SCR$ is maximum at packet size $N_p = 18$, and $N_p = 43$ for *Testdata1*. For a conventional scanner like *GE Vivid E9* the packet size is sixteen, as mentioned in section 3.1. The difference in $SCR$ for packet $N_p = 16$ and the packet giving the maximum $SCR$ is 1.795 dB for systole, and 4.064 dB for diastole.

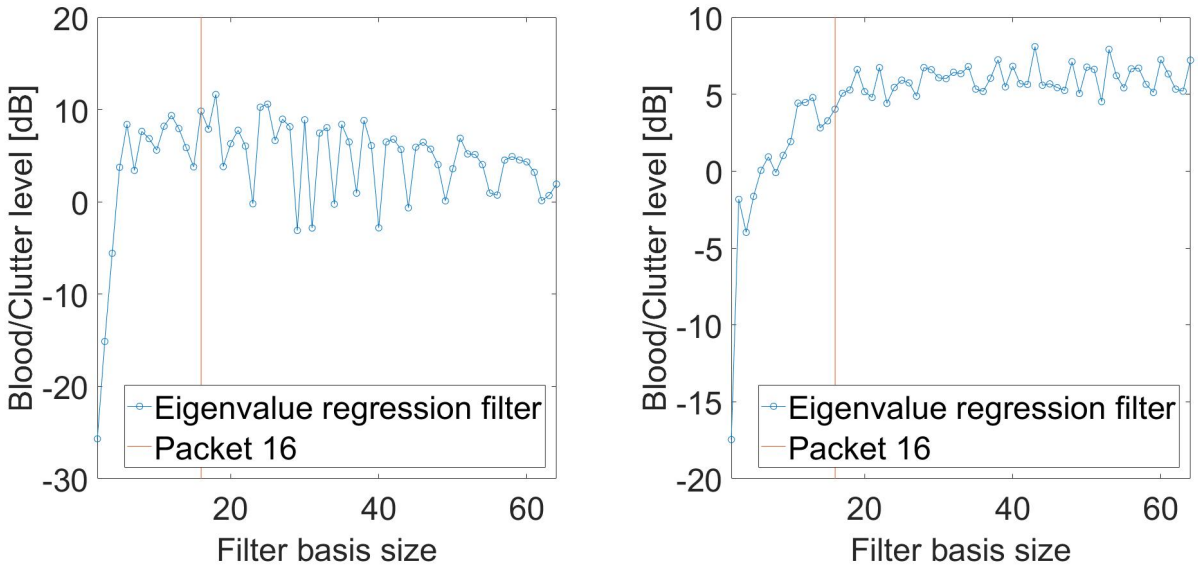


(a) Dataset *Testdata1* at time $t = 0.216\,\mathrm{s}$ in systole. Difference in blood and clutter signal was $0.408\,\mathrm{m/s}$.

(b) Dataset *Testdata1* at time $t = 0.472\,\mathrm{s}$ in diastole. Difference in blood and clutter signal was $0.228\,\mathrm{m/s}$.

Figure 4.15: Effect of increasing the filter basis size on SCR when filtering with the eigenvalue regression filter when blood and clutter signal was sufficiently uncorrelated, for *Testdata1*. The power and velocity threshold were set manually by inspection of the two frames with packet size sixteen.

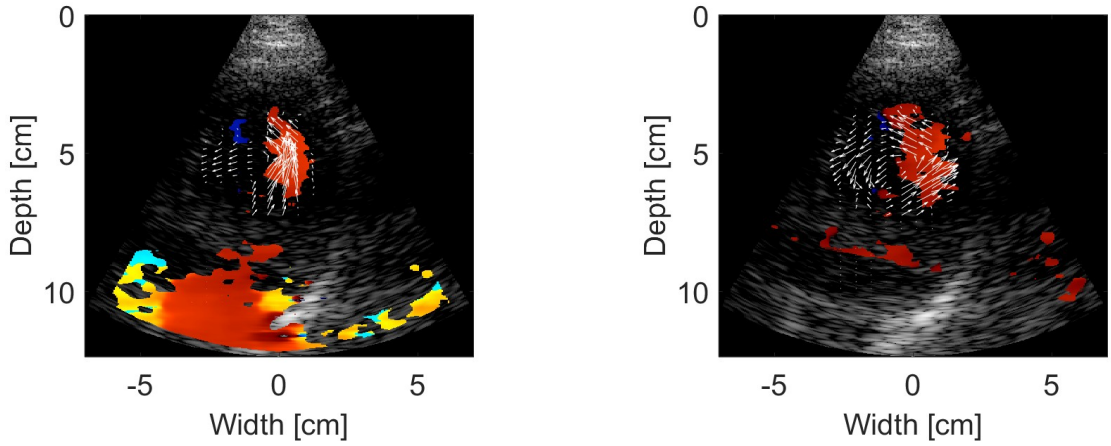


(a) BFI-filter

(b) Eigenvalue Regression filter with manually selected clutter subspace

Figure 4.16: Color flow image with arrows showing the velocity estimate from speckle tracking. Comparison of using the FIR and eigenvalue regression filter to visualize the vortex at time point $t = 0.8360\,\mathrm{s}$, dataset *Testdata2*. Both temporal and spatial averaging were used for the speckle tracking, as explained in section 3.6.

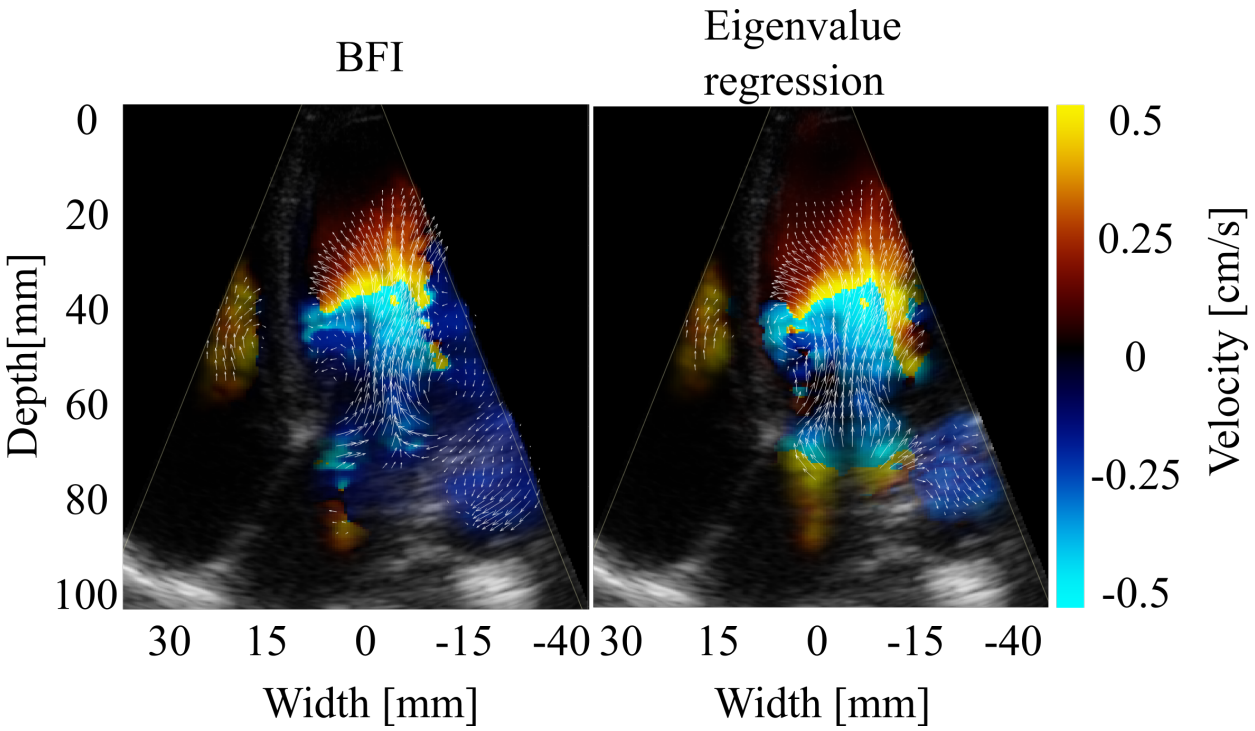


Figure 4.17: Color flow image with arrows showing the velocity estimate from speckle tracking. Comparison of using the FIR (left) and eigenvalue regression filter (right) with the power threshold set manually. For a time point in systole for dataset *Control1*. Both temporal and spatial averaging were used for the speckle tracking, as explained in section 3.6.

The color flow image with arrows from speckle tracking in figure 4.16 shows a vortex formation in the blood flow for *Testdata2* at time $t = 0.8360$ s in diastole. In 4.16a the FIR filter was used and in 4.16b the eigenvalue regression filter was used, where the power threshold was set manually. For this frame the eigenvalue regression filter improves the visualization of the vortex by reducing the tissue flashing at depth 7.5− 15 cm, and reducing blood drop-out at width −2 cm and depth 3− 6 cm.

Figures 4.17 and 4.18 shows the color flow image with arrows from speckle tracking for two frames for dataset *Control1* for the two filters. And, figures 4.19 and 4.20 are from dataset *Patient*. For these frames the clutter subspace for the eigenvalue regression filter was also selected manually. The $PRF$, center frequency $f_0$, probe and scanner used for the recording of these two datasets can be found in table 3.1. For dataset *Control1*, figure 4.17 shows that the visualization of the vortex, located at depth 45 mm and width 5 mm in the left ventricle, is improved when filtering with the eigenvalue regression filter. In figure 4.19, the heart valve can be seen at depth 65 mm and width 10 mm. For this region, the speckle tracking velocity estimate results in chaotic

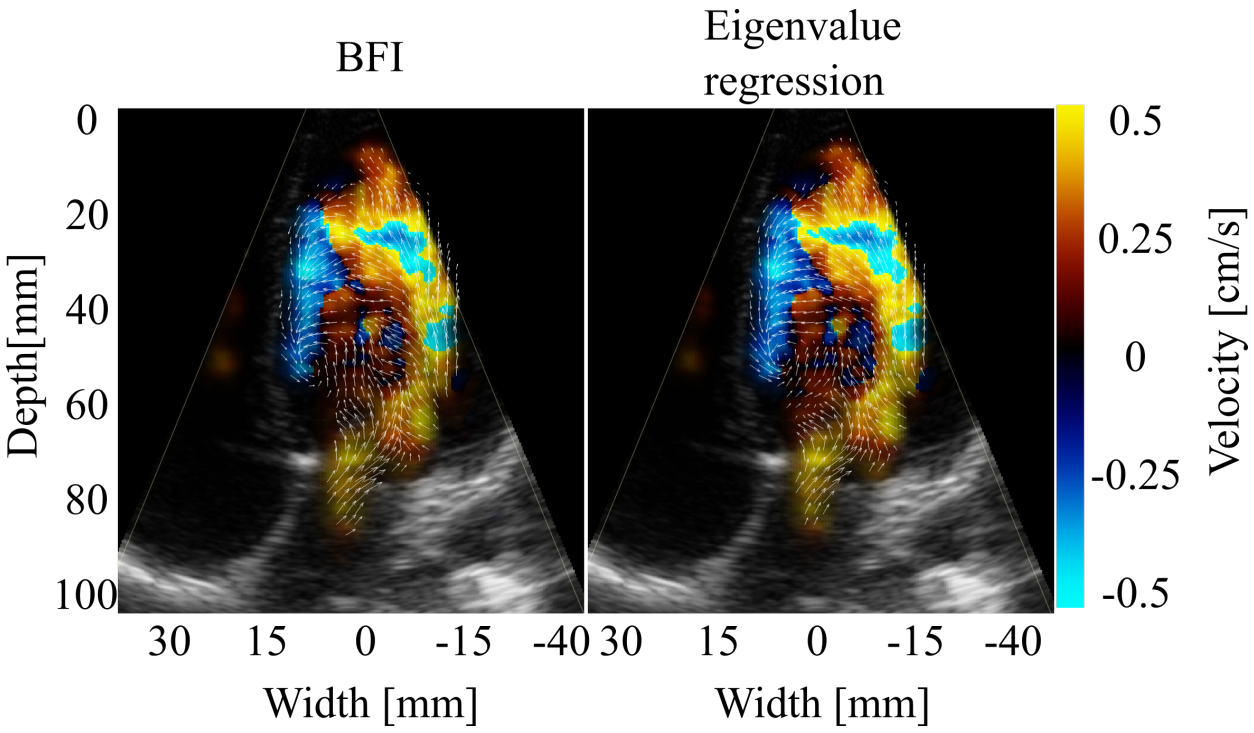


Figure 4.18: Color flow image with arrows showing the velocity estimate from speckle tracking. Comparison of using the FIR (left) and eigenvalue regression filter (right) with the power threshold set manually. For a time point in diastole for dataset *Control1*. Both temporal and spatial averaging were used for the speckle tracking, as explained in section 3.6.

arrows for the FIR filter, and this indicate that the eigenvalue regression filter supresses the signal from the heart valve in a larger extent than the FIR filter. In figure 4.20, using the eigenvalue regression filter results in less blood signal drop-out. The vortex formation for dataset *Patient* in figure 4.20 is located much closer towards the apex in the left ventricle, at depth 35 mm and width −10 mm, than for dataset *Control1* in figure 4.18, at depth 45 mm and width 10 mm.

## 4.3 Investigate the Fundamental Properties of the Eigenvalue Regression Filter for Separating Blood and Clutter signal

Simulations were carried out in order to better understand how the velocity difference affect the correlation between the clutter and blood signals. Three simulations, *Simulation1*, *Simulation2*, and *Simulation5*, was compared to one another. *Simulation1* was of a clutter phantom, *Simulation2* was of a clutter and a blood phantom, where the velocity difference between the

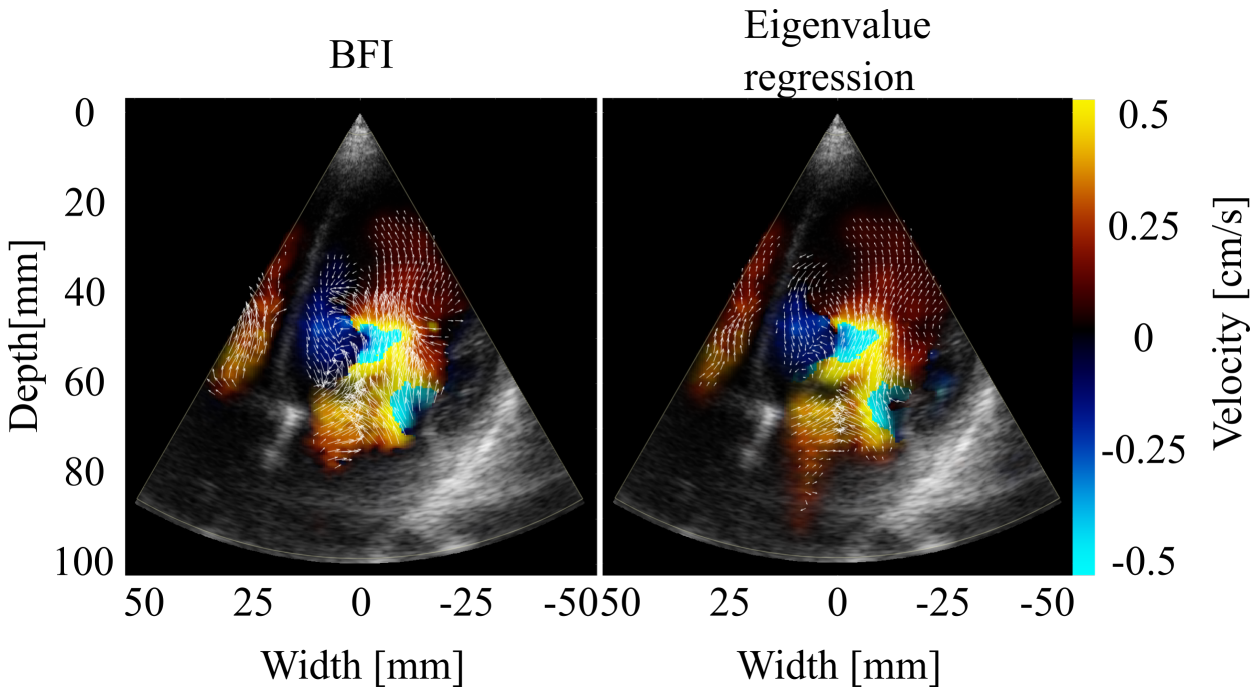


Figure 4.19: Color flow image with arrows showing the velocity estimate from speckle tracking. Comparison of using the FIR (left) and eigenvalue regression filter (right) with the power threshold set manually. For a time point in systole for dataset *Patient1*. Both temporal and spatial averaging were used for the speckle tracking, as explained in section 3.6.

clutter and blood was low, and *Simulation5* was of a clutter and a blood phantom where the velocity difference between the clutter and blood signals was high. The frequency spectrum of these three cases are shown in figure 4.21. The absolute velocity for the clutter was 0.1 m/s in all cases, and the absolute velocity of the blood signal was 0.15 m/s, and 0.3 m/s. Figure 4.22 shows the eigenvalue power. There is no visible difference between figure 4.22a and figure 4.22b even though there is blood signals present in one, and not the other. Therefore, the clutter and blood signal power is contained in the same eigenvalues for *Simulation2*. By comparing *Simulation1* in figure 4.22a with *Simulation5* in figure 4.22c the power of the clutter signal is mostly contained in the first ten eigenvalues, and the power of the blood signal is contained in eigenvalues number eleven to thirty for *Simulation5*. The remaining eigenvalues mostly contain the signal power from the noise signals. Eigenvalues around number fifteen might contain signal power from both clutter and blood signals. The number of eigenvalues representing one velocity is determined by the transit time of the scatterer. Therefore, low velocities would be entirely represented by fewer eigenvectors than high velocities.

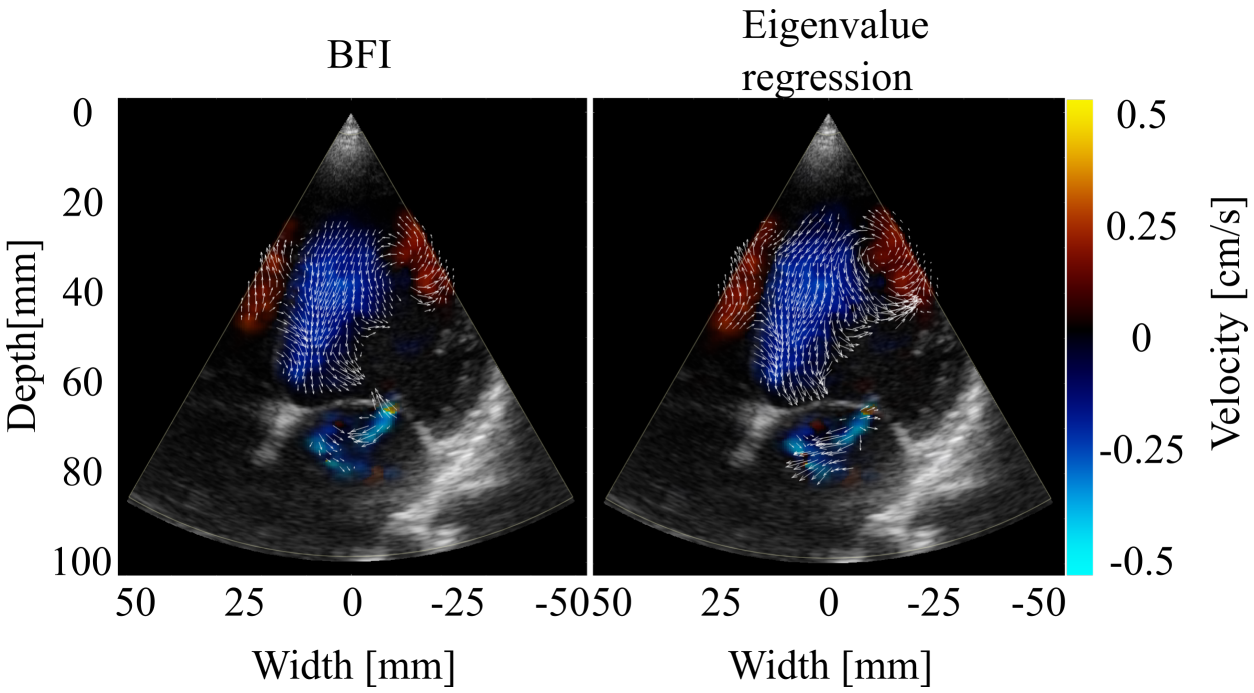


Figure 4.20: Color flow image with arrows showing the velocity estimate from speckle tracking. Comparison of using the FIR (left) and eigenvalue regression filter (right) with the power threshold set manually. For a time point in diastole for dataset *Patient1*. Both temporal and spatial averaging were used for the speckle tracking, as explained in section 3.6.

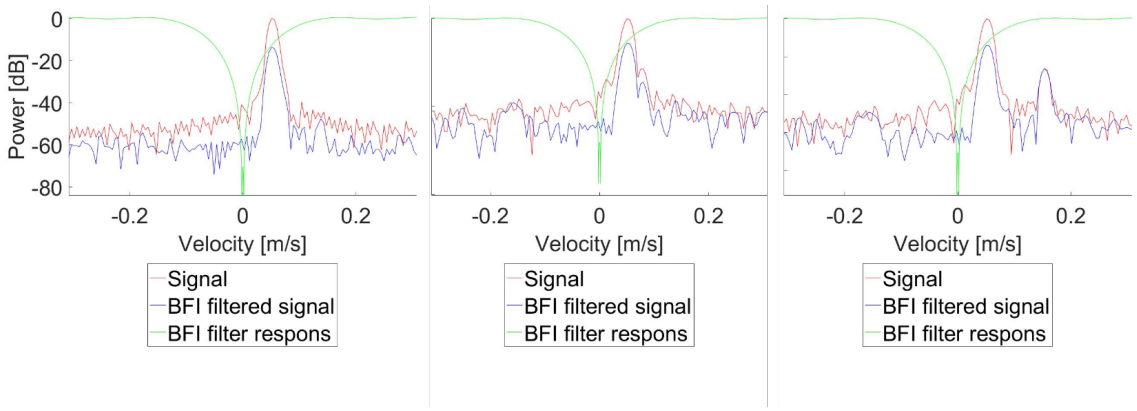


Figure 4.21: Frequency spectrum of *Simulation1* only clutter, *Simulation2* clutter and blood signals with low difference velocity difference, and *Simulation5* clutter and blood signals with a high velocity difference. Frequency spectrum showing the signal, the FIR filter respons and the signal filtered with the FIR filter. Because of the high clutter velocity clutter supression is not sufficient.

Figure 4.23 shows the power distribution of the spectral content of the eigenvectors, as explained in section 3.5. The frequency spectrum of the eigenvectors containing blood signal is distinguishable for *Simulation5* in figure 4.23c. It is visible as broadband signals with center fre-

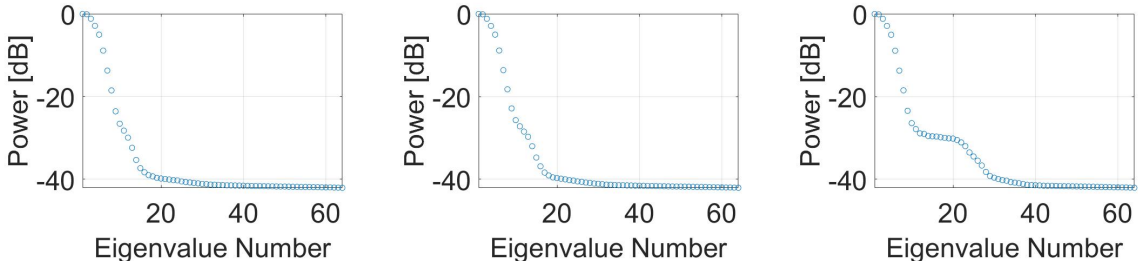


(a) Only clutter signal with absolute velocity of clutter 0.1 m/s

(b) Clutter and blood signal, with absolute velocity of clutter 0.1 m/s and blood 0.15 m/s.

(c) Clutter and blood signal, with absolute velocity of clutter 0.1 m/s and blood 0.3 m/s.

Figure 4.22: Power of eigenvalues of *Simulation1* only clutter, *Simulation2* clutter and blood signals with a low velocity difference, and *Simulation5* clutter and blood signals with a high velocity difference. In (b) bandwidth of the clutter signal is larger than the separation between the clutter and blood signal. The same eigenvectors contain both clutter and blood signal and the blood signal is not possible to separate from the clutter signal. In (c) the clutter and blood signal are separated into different eigenvalues and the eigenvalues corresponding to blood are $10-30$.

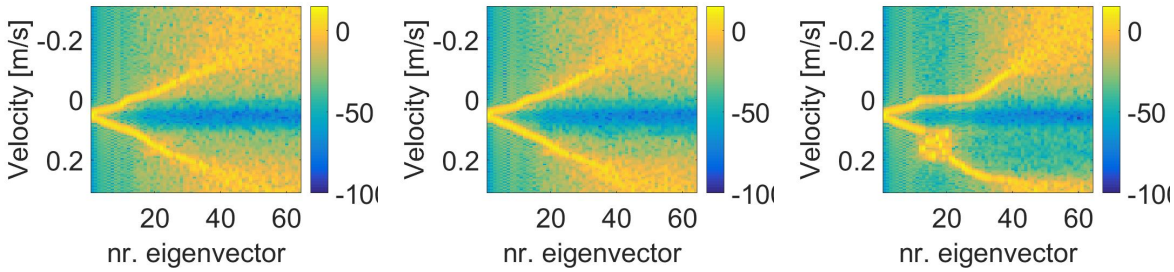


(a) Only clutter signal with absolute velocity of clutter 0.1 m/s

(b) Clutter and blood signal, with absolute velocity of clutter 0.1 m/s and blood 0.15 m/s.

(c) Clutter and blood signal, with absolute velocity of clutter 0.1 m/s and blood 0.3 m/s.

Figure 4.23: Power distribution of the spectral content of the eigenvectors as explained in section 3.5 for *Simulation1* only clutter, *Simulation2* clutter and blood signals with a low velocity difference, and *Simulation5* clutter and blood signals with a high velocity difference. In (c) the eigenvectors with broader bandwidth around eigenvector number fifteen contain the most blood signal.

quency corresponding to 0.15 m/s around eigenvector number fifteen to twenty. The Doppler angle was 60 deg so the axial velocity of the blood scatterers was 0.15 m/s in this case. Figure 4.24 shows B-mode images of the two cases with low and high velocity difference between clutter and blood signals. The data have been filtered using the eigenvalue regression filter with power threshold equal to the $SCR$ at $-25$ dB and velocity threshold equal to the axial tissue ve-

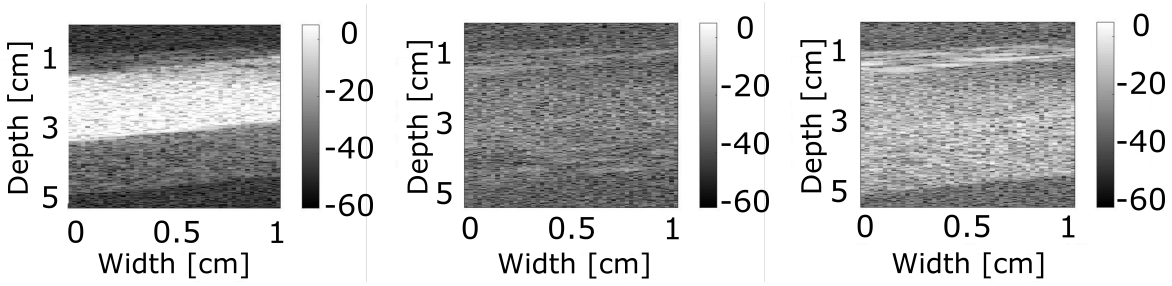


(a) B-mode image of the tube phantom with clutter and blood signal.

(b) B-mode image showing clutterfiltering attempt using the eigenvalue regression filter for *Simulation2* when the clutter and blood signal was correlated. Absolute velocity of clutter 0.1 m/s and blood 0.15 m/s.

(c) B-mode image showing clutterfiltering attempt using the eigenvalue regression filter for *Simulation5* when the clutter and blood signal was sufficiently uncorrelated. Absolute velocity of clutter 0.1 m/s and blood 0.3 m/s.

Figure 4.24: Eigenvalue regression filter used for filtering *Simulation2* and *Simulation5*.

| Part of heart cycle | Clutter [m/s] | | Blood [m/s] | | Difference [m/s] | |
|---|---|---|---|---|---|---|
| | Max. vel. | Sim. par. | Max. vel. | Sim. par. | Max. vel. | Sim. par. |
| Systole (outflow) | 0.116 | 0.15 | 0.489 | 0.5 | 0.373 | 0.35 |
| Diastole (inflow) | 0.13 | | >0.57 | | >0.44 | |
| Diastole (vortex) | 0.03 | 0.03 | 0.19 | 0.15 | 0.16 | 0.12 |

Table 4.1: Parameters used for *Simulation6* and *Simulation7*, and the maximum absolute velocity found by inspection of the sonogram of dataset *Testdata2*.

locity. For comparison figure 4.24a shows the phantom without filtering. For the case with a low difference it was not possible to get sufficient clutter signal attenuation.

Figure 4.25 shows the effect of increasing packet size on the *SCR*. The results were from *Simulation2*, *Simulation3*, *Simulation4*, and *Simulation5*. For these simulations the clutter velocity was 0.1 m/s, and for each simulation the blood velocity was increased. From figure 4.25d the eigenvalue regression filter performs well for both low and high packet size if the velocity difference between blood and clutter signal is high.

Two simulations were performed with parameters corresponding to the ones found in the *in vivo* test data with the highest *PRF*, *Testdata2*. From figure 4.2 there is a delay between the maximum clutter velocity and the maximum blood velocity. The maximum clutter velocity was found by inspection of the sonogram for a ROI in the heart wall, and the maximum blood velocity by inspection of the sonogram with a ROI in the lumen. These sonograms are shown in figure

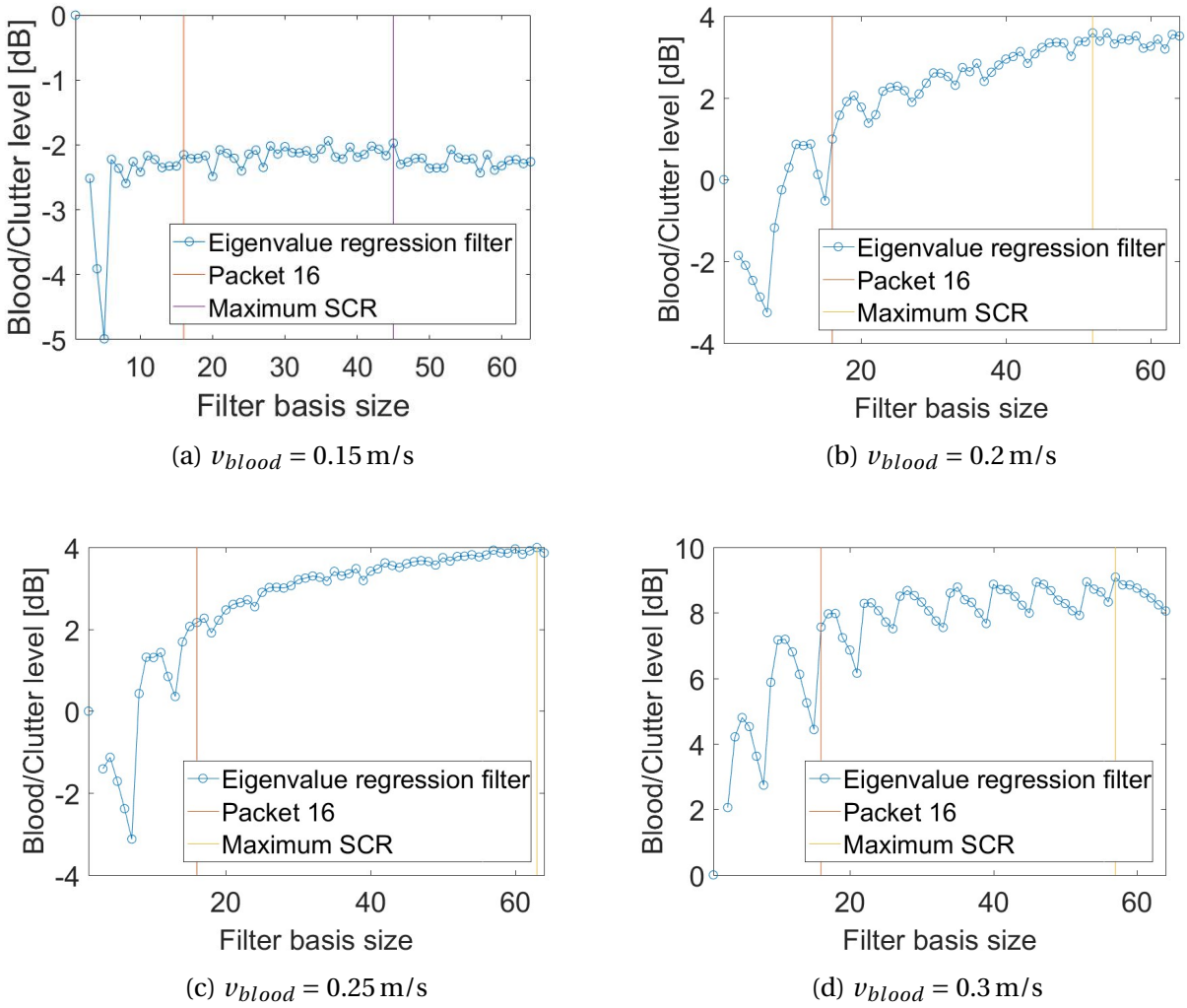


(a) $v_{blood} = 0.15\,\mathrm{m/s}$

(b) $v_{blood} = 0.2\,\mathrm{m/s}$

(c) $v_{blood} = 0.25\,\mathrm{m/s}$

(d) $v_{blood} = 0.3\,\mathrm{m/s}$

Figure 4.25: Optimum packet size for increasing difference between blood and clutter signal. For the simulation the velocity threshold was equal to the axial component of the clutter velocity and the power threshold equal to the $SCR$. The clutter velocity was 0.1 m/s.

4.2 together with a B-mode image showing the ROIs. The maximum clutter velocity in systole is 0.116 m/s, and the maximum blood velocity is 0.489 m/s. The maximum blood velocity might be higher than the Nyquist velocity for a ROI in the lumen closer to the heart valve. The difference in maximum velocity for blood and clutter is 0.373 m/s in systole. In diastole, when there is inflow, the maximum velocity of clutter is 0.13 m/s and the blood velocity is possibly higher than 0.57 m/s. When there is vortex formation the maximum velocity of clutter is 0.03 m/s and the maximum blood velocity is 0.19 m/s, with a difference of 0.16 m/s. These results were used to set parameters for a simulation with constant movement of blood and clutter, *Simulation6*, *Simulation7*. The maximum clutter and blood velocities are summarized in table 4.1 together

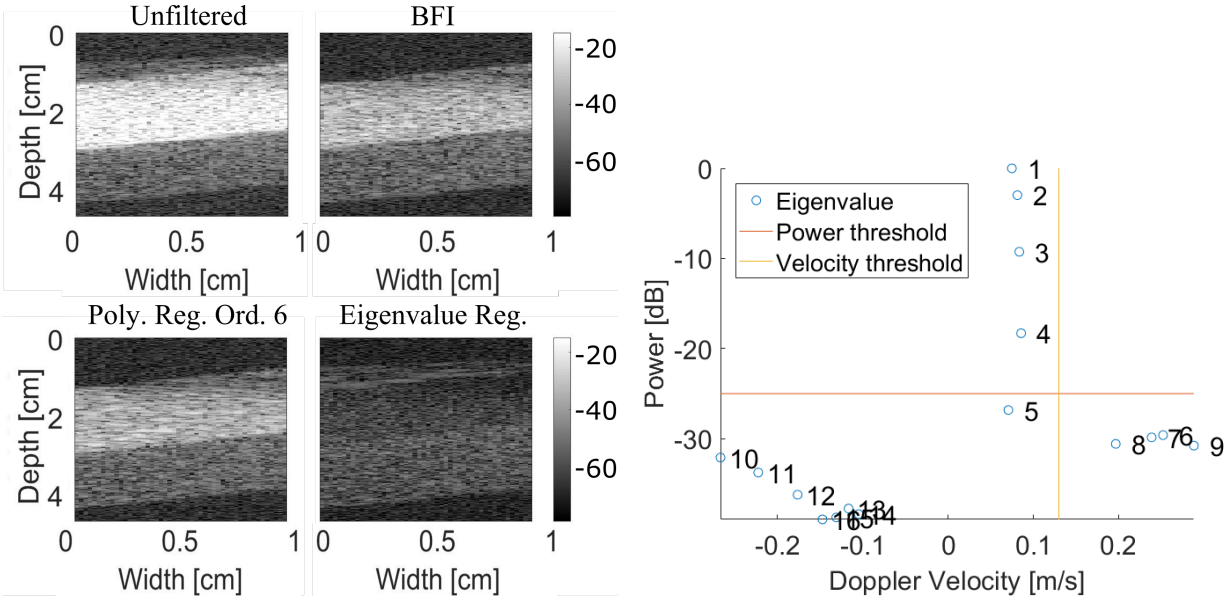


(a) B-mode image showing the tube phantom data after filtering

(b) The eigenvalues and the threshold values selected for the eigenvalue regression filter

Figure 4.26: B-mode images of the data from *Simulation6* filtered with the FIR filter, polynomial regression order six, and with the eigenvalue regression filter. The parameters used for the simulation were set equal to the maximum blood and tissue velocities found in systole for dataset *Testdata2* and are listed in table 4.1. The velocity threshold was set equal to the axial component of the clutter velocity, and the power threshold was set equal to the *SCR*.

with the parameters used for the simulation.

The simulation data from *Simulation6* was filtered with the BFI, polynomial regression filter with order six, and with the eigenvalue regression filter, and are displayed as a B-mode image in figure 4.26a. The threshold values used for the eigenvalue regression filter is shown in figure 4.26b. Similarily for the simulation data from *Simulation7* with parameters from diastole, in figure 4.27a showing the B-mode images, and 4.27b showing the eigenvalues and the threshold values.

The mean *SCR* for the two simulations and the three different filters are listed in table 4.2. The *ROI* of the signal was the whole fast moving tube without the edges and the *ROI* of the clutter signal was the whole slow moving tube without edges. In both instances the *SCR* was highest when filtering with the eigenvalue regression filter.

For the two simulations figure 4.28 and figure 4.29 shows color flow images together with speckle tracking for the FIR and eigenvalue regression filter. In these images using the eigenvalue regression filter results in less tissue flashing and less blood signal drop-out. The mean,

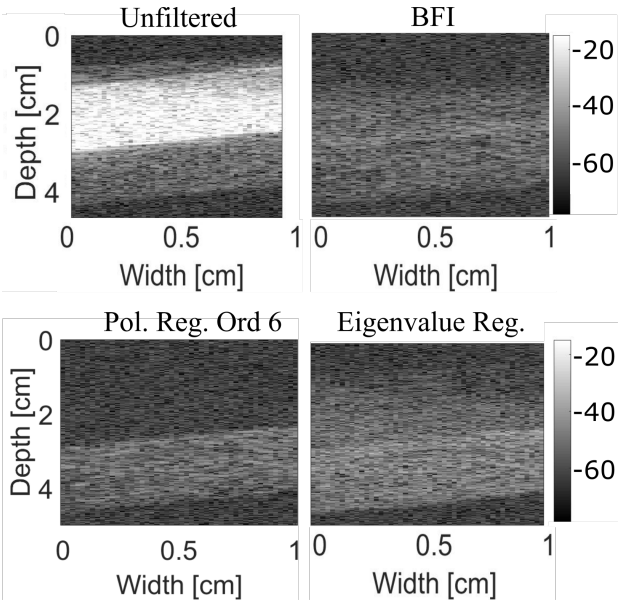


(a) B-mode image showing the tube phantom data after filtering

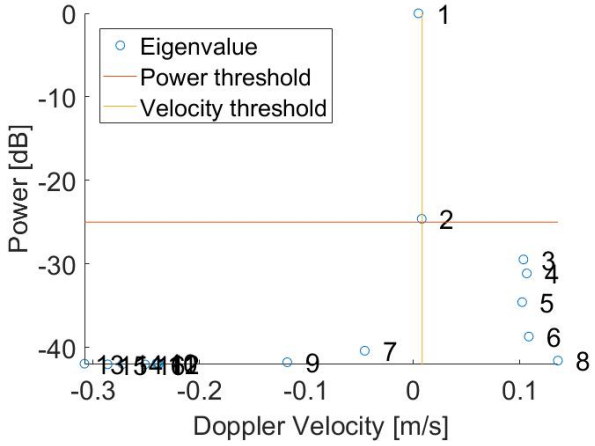


(b) The eigenvalues and the threshold values selected for the eigenvalue regression filter

Figure 4.27: B-mode images of the data from *Simulation7* filtered with the FIR filter, polynomial regression order six, and with the eigenvalue regression filter. The parameters used for the simulation were set equal to the maximum blood and tissue velocities found in diastole for dataset *Testdata2* and are listed in table 4.1. The velocity threshold was set equal to the axial component of the clutter velocity, and the power threshold was set equal to the $SCR$.

standard deviation and bias for the velocity estimates from the speckle tracking are listed in table 4.3.

## 4.4 Investigate the Possibility of Adaptive Basis Order Selection in the Eigenvalue Regression Filter

For the *in vivo* datasets in table 3.1 the different methods for selecting the clutter subspace was tested. Table 4.4 shows these results for a frame in systole, and table 4.5 for a frame in diastole. Green numbers in the tables indicate that the selected clutter subspace was in agreement with the manually selected clutter subspace. The results are also shown in the bar chart in figure 4.30 for systole and 4.31 for diastole. The methods for selecting the clutter subspace are explained in the end of section 2.3. For dataset *Testdata1* and *Testdata2* the manually selected clutter subspace is shown in figures 4.12a, 4.13a, 4.8a and 4.10a. And the clutter subspace $\lambda_{Kc}$ was selected

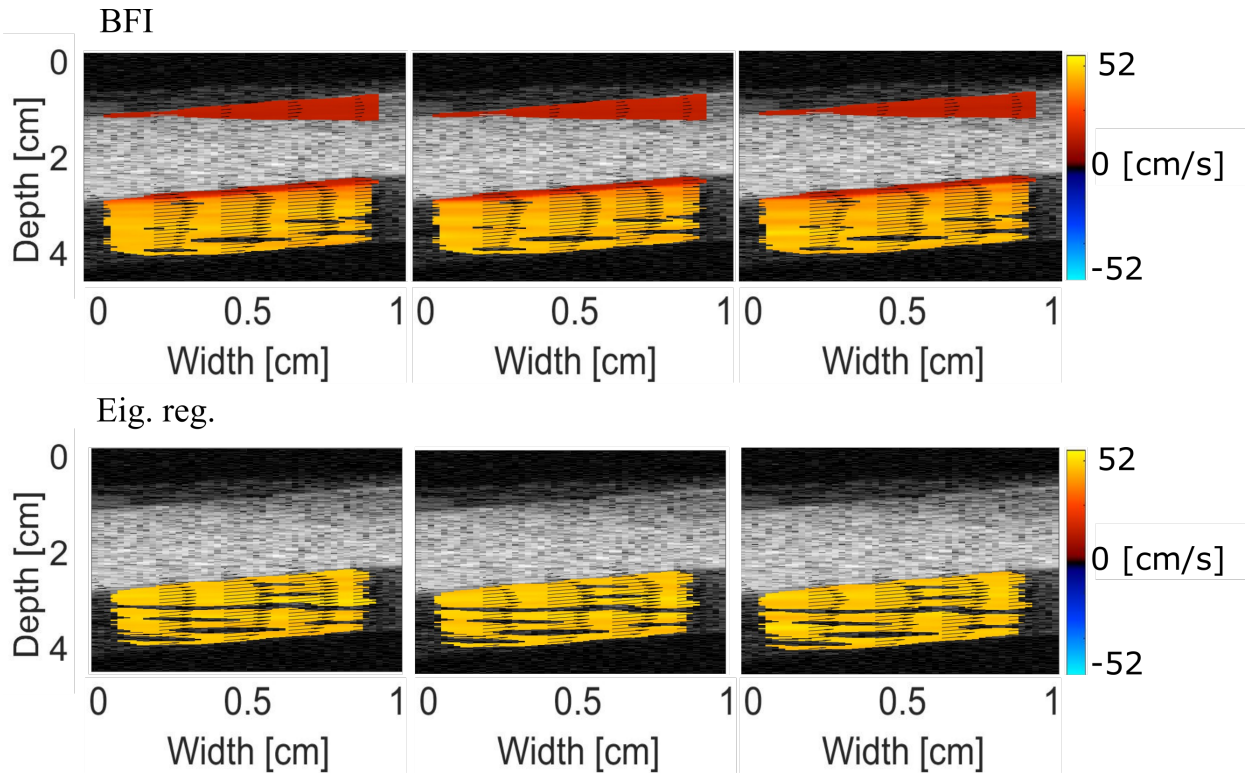


Figure 4.28: Color flow image with arrows from the velocity estimate from speckle tracking of *Simulation6* filtered with FIR filter in top row and the eigenvalue regression filter in the bottow row. The parameters used for the simulation were set equal to the maximum blood and tissue velocities found in systole for dataset *Testdata2* and are listed in table 4.1.

in the same way for the rest of the datasets, by looking at the B-mode images of each eigenvector. The eigenvalues together with the threshold values are shown in figures 4.12b, 4.13b for *Testdata1*, and 4.10b, 4.10b for *Testdata2*.

| Type of filter | SCR [dB] | |
|---|---|---|
| | Systole | Diastole |
| Eigenvalue regression filter | 5.90 | 6.20 |
| FIR filter | -20.11 | -0.02 |
| Polynomial regression filter ord. 6 | -20.48 | 5.56 |

Table 4.2: The *SCR* found after filtering with eigenvalue regression filter, polynomial regression filter with order six and the FIR filter for *Simulation6* with parameters corresponding to the maximum absolute velocity of clutter and blood in systole and *Simulation7* for diastole. The SCR of the tube phantom data was $-25$ dB before filtering. The velocities and simulation parameters are listed in table 4.1.

| Type of filter | Mean velocity [m/s] | | Simulation velocity | | Bias [m/s] | |
|---|---|---|---|---|---|---|
| | Systole | Diastole | Systole | Diastole | Systole | Diastole |
| Eigenvalue regression filter | $0.482 \pm 0.051$ | $0.138 \pm 0.032$ | 0.5 | 0.15 | $-0.0180 \mp 0.051$ | $-0.0120 \mp 0.032$ |
| FIR filter | $0.457 \pm 0.073$ | $0.181 \pm 0.071$ | 0.5 | 0.15 | $-0.0430 \mp 0.051$ | $0.0310 \mp 0.071$ |

Table 4.3: The mean velocity and the bias for the velocity estimate from speckle tracking of *Simulation6* and *Simulation7* filtered with the FIR filter and the eigenvalue regression filter. The parameters used for *Simulation6* were set equal the maximum absolute velocity of blood and tissue found in systole for dataset *Testdata2* and the parameters used for *Simulation7* equal the ones found in diastole. The parameters are listed in table 4.1.

| Dataset | $\lambda_{Kc}$ | Demené | AIC | MDL |
|---|---|---|---|---|
| *Control1* | 5 | 3 | 3 | 4 |
| *Control2* | 5 | 3 | 7 | 8 |
| *Control3* | 2 | 2 | 5 | 7 |
| *Patient1* | 2 | 5 | 5 | 6 |
| *Patient2* | 3 | 2 | 3 | 4 |
| *Patient3* | 1 | 2 | 3 | 6 |
| *Patient4* | 2 | 1 | 5 | 8 |
| *Testdata1* | 10 | 8 | 5 | 7 |
| *Testdata2* | 4 | 3 | 4 | 5 |

Table 4.4: The clutter subspace selected by different methods for a frame in systole for different datasets. Two fully automatic methods based on the AIC, and the MDL, and a semi-automatic method purposed by Demené et al. (2015) using the power of a clutter and blood ROI to select a power threshold. These methods were compared to the manual selected clutter subspace $\lambda_{Kc}$. That was selected based on B-mode images of the eigenvectors. Green numbers indicate that the automatic selection method agree with the manual selected clutter subspace.

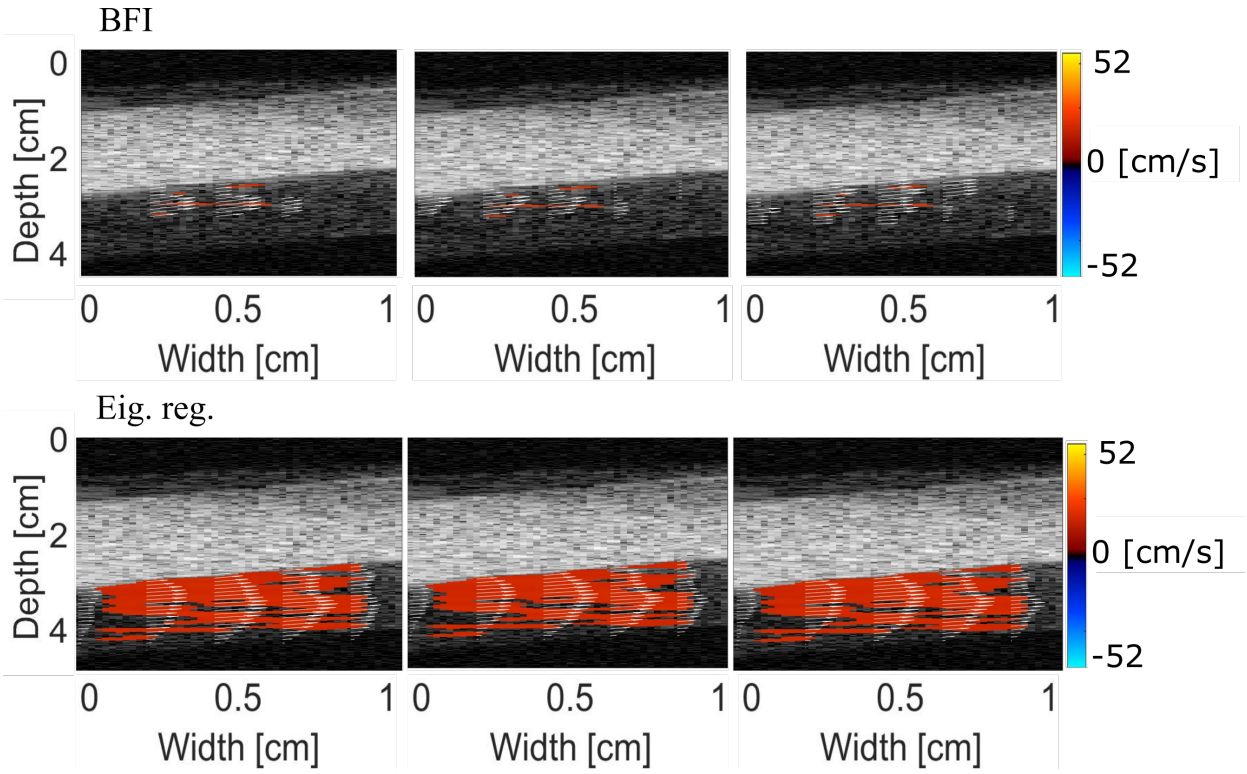


Figure 4.29: Color flow image with arrows from the velocity estimate from speckle tracking of *Simulation7* filtered with FIR filter in top row and the eigenvalue regression filter in the bottow row. The parameters used for the simulation were set equal to the maximum blood and tissue velocities found in diastole for dataset *Testdata2* and are listed in table 4.1.

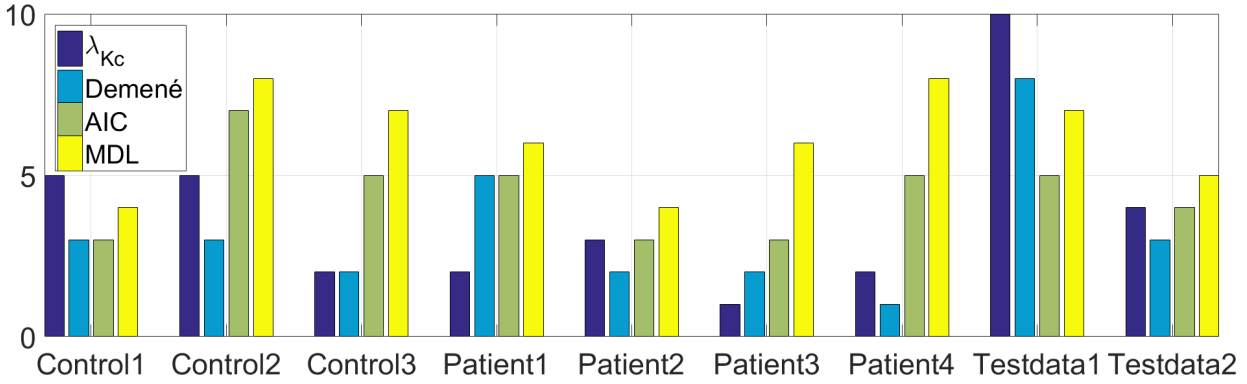


Figure 4.30: Bar chart showing the clutter subspace selected by different methods, for a frame in systole for different datasets. Two fully automatic methods based on the AIC, and the MDL, and a semi-automatic method purposed by Demené et al. (2015) using the power of a clutter and blood ROI to select a power threshold. These methods were compared to the manual selected clutter subspace $\lambda_{Kc}$. This was selected based on B-mode images of the eigenvectors.

| Dataset | $\lambda_{Kc}$ | Demené | AIC | MDL |
|---|---|---|---|---|
| *Control1* | 3 | 3 | 3 | 3 |
| *Control2* | 2 | 2 | 4 | 8 |
| *Control3* | 2 | 2 | 4 | 6 |
| *Patient1* | 2 | 4 | 5 | 6 |
| *Patient2* | 2 | 1 | 3 | 5 |
| *Patient3* | 1 | 2 | 3 | 6 |
| *Patient4* | 2 | 1 | 5 | 7 |
| *Testdata1* | 4 | 3 | 3 | 4 |
| *Testdata2* | 2 | 2 | 3 | 4 |

Table 4.5: The clutter subspace selected by different methods for a frame in diastole for different datasets. Two fully automatic methods based on the AIC, and the MDL, and a semi-automatic method purposed by Demené et al. (2015) using the power of a clutter and blood ROI to select a power threshold. These methods were compared to the manual selected clutter subspace $\lambda_{Kc}$. That was selected based on B-mode images of the eigenvectors. Green numbers indicate that the automatic selection method agree with the manual selected clutter subspace.

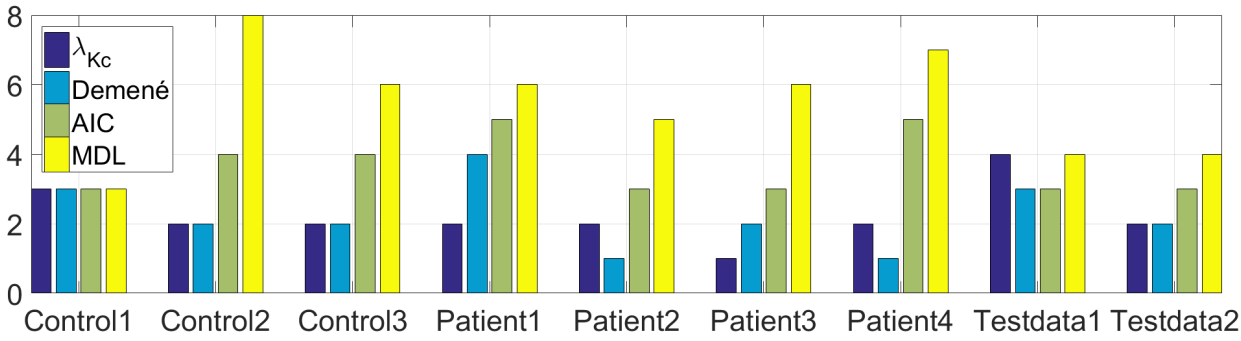


Figure 4.31: Bar chart showing the clutter subspace selected by different methods, for a frame in diastole for different datasets. Two fully automatic methods based on the AIC, and the MDL, and a semi-automatic method purposed by Demené et al. (2015) using the power of a clutter and blood ROI to select a power threshold. These methods were compared to the manual selected clutter subspace $\lambda_{Kc}$. This was selected based on B-mode images of the eigenvectors.

# Chapter 5

# Discussion of Results

Figure 4.7 shows that the FIR filter is not well suited for clutter filtering of cardiac data. From previous research it is possible to achieve proper clutter attenuation using a FIR-filter if the clutter velocity is low, but even better clutter suppression is obtained when using a polynomial regression filter since it has a higher attenuation in the stopband Torp (1997) Bjærum et al. (2002b). This is in agreement with the results because the velocity of the clutter is too high even in diastole, and the attenuation in the stopband is too low to get sufficient clutter suppression. When using this filter for clutter filtering of cardiac data there will be both blood signal drop-outs and tissue flashing in diastole, which makes visualization of the blood vortex difficult.

From the visualization of the eigenvectors in time, figures 4.8, 4.9, 4.10, 4.12, and 4.13, the clutter signal was found to be contained in less eigenvectors during systole than diastole. The clutter subspace is determined by the mean axial velocity, the velocity bandwidth of the clutter signal, and the difference in velocity between clutter and blood signal, Yu and Løvstakken (2010). This agrees with the results since the sonogram in figures 4.1 and 4.2 shows that the bandwidth of the clutter velocity is larger in systole than in diastole.

Clutter was contained in the eigenvectors with highest eigenvalues, blood signal in the eigenvectors with intermediate eigenvalues, and noise in the eigenvectors with lowest eigenvalues. The clutter signal will be contained in the dominant eigenvector. Since the eigenvalue regression filter is a two-dimensional filter it does not matter where the clutter signal is dominant as long as it is dominant somewhere in the signal, Ledoux et al. (1997). Eigenvectors corresponding to clutter signal were typically easy to distinguish from the blood and noise signals. However,

it was difficult to distinguish between eigenvectors representing blood and noise signals since they were both characterized by a range of Doppler velocities from zero to the Nyquist velocity and low eigenvalues. This is in agreement with previous research by Ledoux et al. (1997) that the eigenvalues corresponding to noise do not form such a distinct group as those representing clutter. The similar appearance of blood and noise signals is also shown in figure 4.11, and there is a smooth transition between eigenvectors corresponding to blood and noise.

In figure 4.12 it was not possible to distinguish which eigenvectors contained most of the blood signal because the $PRF$ was too low. The $PRF$ determines the clutter suppression achieved by the eigenvalue regression filter since it limits maximum measureable velocity, and thereby limits the velocity difference of clutter and blood signal. If both the measured clutter and blood velocity are equal to the Nyquist velocity, then those two signals are correlated. From the visualization of the eigenvectors in figure 4.12a, eigenvector number eleven looked like it contained only blood signal. However, when filtering using eigenvectors one to ten as clutter subspace the speckle pattern was stationary over one packet from a video of B-mode images, and it is therefore a possibility that eigenvectors eleven to sixteen only contain noise signals even though it has the appearence of blood signal in B-mode images.

Figure 4.14a shows the power distribution of the spectral content of the eigenvectors for *Testdata1*. The image for systole shows that the eigenvectors either contain clutter or noise. The clutter signals are contained in eigenvectors one to ten for packet size sixteen, and one to twenty for packet size sixty four. The remaining power is distributed on all frequencies and are likely noise signals. For diastole the eigenvectors that contain the most blood signals are five to twelve for packet sixteen, and ten to fifty for packet sixty four. These eigenvectors have a larger bandwidth than eigenvectors containing mostly clutter signals, and this is as expected, since blood has a higher velocity than clutter, and therefore shorter transition time which gives a broader bandwidth. The eigenvectors containing blood also had a narrower bandwidth than those containing mostly noise, which is also expected, since the noise is assumed to contain all frequencies. For figure 4.14b one packet contained all temporal signals, and clutter filtering was no longer possible. Clutter filtering is possible if the consecutive signals in one packet are correlated. This way, the clutter signals can be described with a finite number of subsignals. In practice, a packet shorter than 10 ms should be used to achieve correlated signals also for

systole. For low clutter velocities a longer packet can be applied Ledoux et al. (1997). This was also in agreement with the results in figure 4.15 which showed that for systole the maximum *SCR* was achieved by using a packet of eighteen, which is 9 ms. For diastole, longer packets improved the *SCR*. The eigenvalue regression filter also attenuated the clutter signal for packet size sixteen, and the improvement to the *SCR* by increasing the packet size beyond sixteen for diastole was 4 dB.

Speckle tracking examples from *in vivo* data are shown in figure 4.16, 4.17, 4.18, 4.19, 4.20. The clutter subspace for the eigenvalue regression filter was chosen manually. For figure 4.16 the clutter subspace was chosen using the method purposed by Demené et al. (2015), but for this frame this was the same clutter subspace as the manually selected clutter subspace. Figure 4.19 shows chaotic arrows at width 10 mm and depth 65 mm for the FIR filter, and not for the eigenvalue regression filter. This indicate that the eigenvalue regression filter better supress signals from the heart valve than the FIR filter. In these examples, using the eigenvalue regression filter results in less tissue flashing and blood signal drop-outs compared to the FIR filter. And, in these examples, the eigenvalue regression filter improves the visualization of the vortex formation of blood in systole and diastole compared to the FIR filter.

The results in figure 4.18 and 4.20 showed that the vortex formation was much closer to the apex for the patient with dilated cardiomyopathy compared to the healthy control. This is in agreement with Hong et al. (2008), that dilated cardiomyopathy effect the location of the left ventricle vortex. However, the duration of the vortex is also of importance and was not investigated in this work, and thorough clinical studies are needed to reach any conclusions.

From this work it was experienced that setting a power threshold was easier than setting a velocity threshold for the *in vivo* data. Setting a velocity threshold equal the mean velocity from all spatial points in one image severly underestimated the true clutter velocity. It was also easier to distinguish between clutter and blood, than blood and noise, therefore using the eigenvalue regression filter to also subtracting the noise signal was not looked further into.

From *Simulation1*, *Simulation2* and *Simulation5* it was found that when the clutter and blood velocity difference is low, and even though the two signals are distinguishable in the frequency spectrum, figure 4.21, their eigenvectors are impossible to distinguish from one another, figure 4.22, 4.23 and filtering with the eigenvalue regression filter is not possible, figure 4.24.

This is because the clutter and blood velocity difference determine the amount of correlation between the signals Ledoux et al. (1997).

In order to determine whether this was an issue for the *in vivo* data *Testdata2*, the maximum estimated axial velocity for clutter and blood for a frame in systole and a frame in diastole was used to determine the parameters in *Simulation6* and *Simulation7*. The parameters are listed in table 4.1, and the results are listed in table 4.2 and figure 4.26 for systole and figure 4.27 for diastole. These simulations showed that the difference between blood og clutter signals were high enough, and that they were mostly represented by different eigenvectors. However, in the simulation the blood and clutter velocities had a constant velocity profile, and for the *in vivo* data the velocity profiles are more complex.

The results from *Simulation6* and *Simulation7* also showed increase in the *SCR* for filtering with the eigenvalue regression filter compared to the polynomial regression filter and the FIR filter. This is in agreement with previous research showing that eigenvalue regression filters can more effectively suppress clutter in CFI scenarios with substantial tissue motion Yu and Løvstakken (2010). Also, eigenvalue regression filter can better adapt to the Doppler signal characteristics Yu et al. (2007), and is suitable as a clutter filter Ledoux et al. (1997) Kargel et al. (2003), also for both low and high clutter velocity Song et al. (2006). It has also been shown that the eigenvalue regression filter is very effective at removing the clutter with and without clutter movement Kruse and Ferrara (2002).

For a given high clutter velocity and varying blood velocity, the *SCR* was improved by increasing the packet beyond packet sixteen from figure 4.25. The improvement was most evident when the difference between clutter and blood was equal the clutter velocity. When the difference between the clutter and blood velocity was high, the eigenvalue regression achieved a high *SCR* also for packet size sixteen. This is in agreement with previous research showing that an increase in packet size decreases the correlation between clutter and blood signal. The correlation between clutter and blood signals increases with decreasing difference between the clutter and blood velocity, Ledoux et al. (1997). However, there was no improvement when the difference between the clutter and blood velocity was half the clutter velocity, and this is not in agreement with previous *in vitro* phantom study by Demené et al. (2015), that the eigenvalue regression filter performance is increasing with the packet size used in estimating the correlation matrix.

In the study by Demené et al. (2015) a high $SCR$ of 6 dB was obtained for a difference in clutter and blood velocity as low as 4 % of the clutter velocity when both a large amount of temporal and spatial samples were used in the estimation of the correlation matrix. The main differences of the simulations in this work and the *in vitro* phantom study is that the clutter and blood velocity direction was equal in the simulation and different in that of Demené et al. (2015). The velocities in the *in vitro* phantom study were also five times lower than in the simulations in this work. In the *in vitro* study by Demené et al. (2015) it was noted that those results remain to be verified in high motion applications such as cardiac imaging.

Figures 4.28, and 4.29 shows speckle tracking images for *Simulation6* with parameters from systole, and *Simulation7* with parameters from diastole. Using the eigenvalue regression filter instead of the FIR filter reduces tissue flashing in systole and reduces blood signal drop-outs in diastole. From table 4.3 the bias of the velocity estimates from speckle tracking is also smaller for filtering with the eigenvalue regression filter compared to the FIR filter. Previous reseach has found that FIR clutter filter removed both blood and wall signal, resulting in severe underestimation of the blood flow from speckle tracking Gallippi and Trahey (2002).

Tables 4.4 and 4.5, and figures 4.30 and 4.31, shows the results of three of the clutter subspace selection methods mentioned in section 1.1. There are nine datasets and two frames for each dataset yielding eighteen different frames. Since a random selection of clutter subspace would have a 1/16 chance of being correct, it is therefore likely that each of the methods should have at least one correct. Even though it may be beneficial to develop an algorithmic way of choosing the clutter subspace, Yu and Løvstakken (2010), Demené et al. (2015) argue that the adjustment of the power threshold is not as critical as the choise of cut off frequency in conventional filters. The reduction to the $SCR$ by using a suboptimal clutter subspace was not considered, therefore only the methods selecting a clutter subspace that is spot on is indicated with green in the tables.

The method purposed by Demené et al. (2015) selected the clutter subspace correctly in 44 % of the frames from the different datasets in diastole. In systole the AIC method selected correctly in most instances, but it was only correct 22 % of the frames from the different datasets. Wax and Kailath (1985) found that the MDL method provides more consistent estimates, specifically when the packet size is small, which is the case for pulsed-wave Doppler ultrasound. Yu and Cobbold (2006) showed that the AIC and MDL underestimate the clutter subspace in sys-

tole, and overestimate the clutter subspace in diastole. The results presented here suggest that both the AIC and the MDL are overestimating the clutter subspace, both for systole and diastole. For *Testdata1* the MDL and AIC are underestimating the clutter subspace for the frame in systole, but for this frame the blood and clutter signals were correlated and it was quite difficult to choose the clutter subspace manually. The main problem with this dataset was the low $PRF$ as discussed previously. The gap between the clutter subspace selected by the MDL, AIC, and the manually selected clutter subspace is larger for the datasets with a beam aquisition, than for the datasets with a plane wave aquisition. The eigenvalues were calculated using the whole image as the ROI for all the datasets, also the datasets with beam aquisition, and this could be a source of error. For the control and patient datasets the heartrate was high and there were few frames in each heart cycle. It was therefore more difficult to decide which frames showed systole and diastole, and this is also a source of error.

When calculating the AIC and MDL the blood signals are assumed to be gaussian random processes, with zero mean, Wax and Kailath (1985). Although it is generally excepted that the signal from blood cells with random positions in space will sum up incoherently and therefore can be modeled as a Gaussian process, it is not certain that the mean is zero. This might be the reason why the AIC and MDL does not yield more correct clutter subspaces for this application. Perhaps more realistic blood phantoms of the heart could give insight to the probability distribution, and aid in development of the clutter subspace selection method.

This work has been a first step in order to develop a robust fully automatic method for selection of the clutter subspace in eigenvalue regression filters for use with cardiac data. No new method for selecting clutter subspace is suggested in this thesis. Only three of the clutter subspace selection methods mentioned in section 3.4 was implemented and tested with the nine different datasets. And, only two frames in each dataset were considered. Each of the simulations was only carried out once, and the simulations were simple with just two different velocities with plug flow. It is also possible to use eigenvalue regression filters to suppress noise signals, but this was not considered in this work. Neither was it considered to set a Doppler velocity threshold to select the clutter subspace. In this work the opinion of clinicians were not aquired.

# Chapter 6

# Conclusion and Further Work

## 6.1 Conclusion

The eigenvalue regression filter with a manually selected clutter subspace has the possibility of improving the visualization of vortex formation in blood compared to a FIR filter for cardiac data. However, the improvement was not judged by clinicians, and only five different frames were considered. These frames were from three different *in vivo* datasets.

When using the eigenvalue regression filter with a manually selected clutter subspace it is possible to achieve a $SCR$ comparable in strength to that achieved by using a FIR filter for packet size sixteen. The results from the simple simulations showed that the eigenvalue regression filter can reduce the bias in the velocity estimate from speckle tracking compared to a FIR filter, as it reduces tissue flashing, and blood signal drop-outs.

The semi-automatic power threshold select the clutter subspace correctly in 44 % of the frames in diastole considered in this work, but only one frame from nine different datasets were considered. The semi-automatic power threshold is not a practical solution since a region containing clutter and blood signals must be chosen manually.

## 6.2 Further work

Some suggations for further work are to develop a more robust clutter subspace selection method, and evaluation of the previously suggested methods. Input from clinicians is also necessary

when evaluating the method. Possible approaches could include more sophisticated simulations, and *in vitro* experiments using more realistic cardiac phantoms. Possible simulations could include accelerated clutter, expanding clutter, and simulations with different direction for clutter and blood movement. Simulations should also include more realistic blood and tissue phantoms like carotid artery simulations Swillens (2010). To investigate the use of eigenvalue regression filters with accelerated flow it is perhaps an easier approach to use *in vitro* phantoms than simulations as many frames are necessary to get sufficient increase in velocity when using a high $PRF$.

The computation complexity should be considered as many of the previously suggested methods include calculating a cost function for each possible clutter subspace, and that is perhaps not a practical solution for high packet sizes. An other interesting approach is to use machine learning for determining the clutter subspace by recognizing patterns in plot of the eigenvalues.

There are also other types of adaptive clutter filters, like downmixing filters, and these should also be considered and compared to the eigenvalue regression filter for this application.

# Appendix A

# Acronyms

**US** Ultrasound

**CFI** Color flow imaging

**PRF** Pulse repetition frequency

**RF** Radio frequency

**FIR** Finite impulse response

**ROI** Region-of-interest

**BPM** Beats per minute

**FFT** Fast fourier transform

**SCR** Signal-to-clutter ratio

**PCA** Principal component analysis

**DKLT** Discrete Karhunen-Loève transform

**AIC** Akaike information criterion

**MDL** Minimum description length

**BFI** Blood flow imaging

# Bibliography

Achiron, R., Glaser, J., Gelernter, I., Hegesh, J., and Yagel, S. (1992). Extended fetal echocardiographic examination for detecting cardiac malformations in low risk pregnancies. *British Medical Journal*.

Allam, M. E., Kinnick, R. R., and Greenleaf, J. F. (1996). Isomorphism between pulsed-wave doppler ultrasound and direction-of-arrival estimation - part ii: Experimental results. *IEEE Transactions on Ultrasonics, Ferroelectrics, and Frequency Control*.

Benavidez, O. J., Gauvreau, K., Jenkins, K. J., and Geva, T. (2008). Diagnostic errors in pediatric echocardiography: Development of taxonomy and identification of risk factors. *Circulation*.

Bjærum, S. and Torp, H. (1997). Optimal adaptive clutter filtering in color flow imaging. *IEEE Ultrasonics Symposium*.

Bjærum, S., Torp, H., and Kristoffersen, K. (2002a). Clutter filers adapted to tissue motion in ultrasound color flow imaging. *IEEE Transactions on Ultrasonics, Ferroelectrics, and Frequency Control, vol. 49*.

Bjærum, S., Torp, H., and Kristoffersen, K. (2002b). Clutter filter design for ultrasound color flow imaging. *IEEE Transactions on Ultrasonics, Ferroelectrics, and Frequency Control*.

Bohs, L. N., Geiman, B. J., Anderson, M. E., Gebhart, S. C., and Trahey, G. E. (2000). Speckle tracking for multi-dimensional flow estimation. *Ultrasonics, vol. 38,*.

Brown, K. L., Ridout, D. A., Hoskote, A., Verhulst, L., Ricci, M., and Bull, C. (2006). Delayed diagnosis of congenital heart disease worsens preoperative condition and outcome of surgery in neonates. *Heart*.

Candès, E. J., Li, X., Ma, Y., and Wright, J. (2005). Robust principal component analysis? *J. ACM JACM, vol. 58, no. 3*.

Demené, C., Deffieux, T., Pernot, M., Osmanski, B.-F., Biran, V., Gennisson, J.-L., Sieu, L.-A., Bergel, A., Franqui, S., Correas, J.-M., Cohen, I., Baud, O., and Tanter, M. (2015). Spatiotemporal clutter filtering of ultrafast ultrasound data highly increases doppler and fultrasound sensitivity. *IEEE Transactions on Medical Imaging, vol. 34, no. 11*.

Donoho, D. and Gavish, M. (2014). Minimax risk of matrix denoising by singular value thresholding. *The Annals of Statistics, vol. 42, no. 6*.

Dunmire, B., Beach, K. W., Labs, K., Plett, M., and Strandness, D. E. (2000). Cross-beam vector doppler ultrasound for angle-independent velocity measurements. *Ultrasound in Medicine & Biology, vol. 26,*.

Eapen, R. S., Rowland, D. G., and Franklin, W. H. (1998). Effect of prenatal diagnosis of critical left heart obstruction on perinatal morbidity and mortality. *American Journal of Perinatology*.

Faurie, J., Baudet, M., Assi, K. C., Auger, D., Gilbert, G., Tournoux, F., and Garcia, D. (2017). Intracardiac vortex dynamics by high-frame-rate doppler vortography - in vivo comparison with vector flow mapping and 4-d flow mri. *IEEE Transactions on Ultrasonics, Ferroelectrics, and Frequency Control, vol. 64, no. 2*.

Ferrara, K. and DeAngelis, G. (1997). Color flow mapping. *Ultrasound in Medicine & Biology, Vol 23, Issue 3*.

Fort, A., Manfredi, C., and Rocchi, S. (1995). Adaptive svd-based ar model order determination for time-frequency analysis of doppler ultrasound signals. *Ultrasound in Medicine & Biology, vol. 21, no. 6*.

Gallippi, C. M. and Trahey, G. E. (2002). Adaptive clutter filtering via blind source separation for two-dimensional ultrasonic blood velocity measurement. *Ultrasonic Imaging, vol. 24*.

Gharib, M., Rambod, E., Kheradvar, A., Sahn, D. J., and Dabiri, J. O. (2006). Optimal vortex formation as an indec of cardiac health. *Proceeding of the National Academy of Sciences of the United States of America, vol 103,*.

Hoeks, A. P. G., van de Vorst, J. J. W., Dabekaussen, A., Brands, P. J., and Reneman, R. S. (1991). An efficient algorithm to remove low frequency doppler signals in digital doppler systems. *Ultrasonic Imaging, Volume 13, Issue 2*.

Hong, G.-R., Pedrizzetti, G., Tonti, G., Li, P., Wei, Z., Kim, J. K., Baweja, A., Liu, S., Chung, N., Houle, H., Narula, J., and Vannan, M. A. (2008). Characterization and quantification of vortex flow in the human left ventricle by contrast echocardiography using vector particle image velocimetry. *JACC Cardiovasc. Imaging*.

Jensen, J. (1996). Field: A program for simulating ultrasound systems. *Med. Biol. Comput., vol. 34*.

Kargel, C., Höbenreich, G., Trummer, B., and Insana, M. F. (2003). Adaptive clutter rejection filtering in ultrasonic strain-flow imaging. *IEEE Transactions on Ultrasonics, Ferroelectrics, and Frequency Control, vol. 50*.

Kasai, C., Namekawa, K., Tsukamoto, M., and Koyano, A. (1983). Realtime bloodflow imaging system utilizing auto-correlation techniques. *Ultrasound in Medicine & Biology, 2, 203-8,*.

Kruse, D. E. and Ferrara, K. W. (2002). A new high resolution color flow system using an eigendecomposition-based adaptive filter for clutter rejection. *IEEE Transactions on Ultrasonics, Ferroelectrics, and Frequency Control, vol. 49*.

Landis, B. J., Levey, A., Levasseur, S. M., Glickstein, J. S., Kleinman, C. S., Simpson, L. L., and Williams, I. A. (2013). Prenatal diagnosis of congenital heart disease and birth outcomes. *Pediatric Cardiology, vol. 34*.

Ledoux, L. A. F., Brands, P. J., and Hoeks, A. P. G. (1997). Reduction of the clutter component in doppler ultrasound signals based on singular value docomposition: a simulation study. *Ultrasonic Imaging, vol. 19*.

Mahle, W. T., Clancy, R. R., McGaurn, S. P., Goin, J. E., and Clark, B. J. (2001). Impact of prenatal diagnosis on survival and early neurologic morbidity in neonates with the hypoplastic left heart syndrome. *Pediatrics*.

Manolakis, D. G. and Ingle, V. K. (2011). *Applied Digital Signal Processing*. Cambridge University Press.

Pearson, K. (1901). On lines and planes of closest fit to systems of points in space. *Philosophical Magazine vol 2*.

Pedrizzetti, G., La Canna, G., Alfieri, O., and Tonti, G. (2014). The vortex - an early predictor of cardiovascular outcome? *Nature Reviews Cardiology*.

Rajiah, P., Mak, C., Dubinksy, T. J., and Dighe, M. (2011). Ultrasound of fetal cardiac anomalies. *American Journal of Roentgenology*.

Reid, J. M. and Spencer, M. P. (1972). Ultrasonic doppler technique for imaging blood vessels. *Science, 176, 1235-6*.

Song, F., Zhang, D., and Gong, X. (2006). Performance evaluation of eigendocomposition-based adaptive clutter filter for color flow imaging. *Ultrasonics, vol. 44*.

Swillens, e. a. (2010). Simulation environment for vascular imaging with ultrasound. Technical report, Mobius Medical Systems.

Therrien, C. W. (1992). *Discrete Random Signals and Statistical Signal Processing*. Prentice Hall, Inc.

Torp, H. (1997). Clutter rejection filter in color flow imaging: A theoretical approach. *IEEE Transactions on Ultrasonics, Ferroelectrics, and Frequency Control, vol. 44, no. 2*.

Trahey, G. E., Allison, J. W., and Von Ramm, O. T. (1987). Angle independent ultrasonic detection of blood flow. *IEEE Transactions on Biomedical Engineering, vol. 34, no. 12*.

Trefethen, L. N. (2008). Householder triangularization of a quasimatrix. *IMA Journal of Numerical Analysis*.

Tzifa, A., Barker, C., Tibby, S. M., and Simpson, J. M. (2007). Prenatal diagnosis of pulmonary atresia: impact on clinical presentation and early outcome. *Archives of disease in childhood. Fetal and neonatal edition*.

van der Linde, D., Konings, E. E. M., Slager, M. A., Witsenburg, M., Helbing, W. A., Takkenberg, J. J. M., and Roos-Hesseling, J. W. (2011). Birth prevalence of congenital heart disease worldwide. *Journal of the American College of Cardiology, vol. 58, no. 21*.

Verhejien, P. M., Lisowski, L. A., Stoutenbeek, P., Hitchcock, J. F., Brenner, J. I., Copel, J. A., Kleinman, C. S., Mejiboom, E. J., and Bennink, G. B. (2001). Prenatal diagnosis of congenital heart disease affects preoperative acidosis in the newborn patient. *The journal of thoracic and cardiovascular surgery*.

Wax, M. and Kailath, T. (1985). Detection of signals by information theoretic criteria. *IEEE Transactions on Acoustics, Speech, and Signal Processing, vol. 33, no. 2*.

Yagel, S., Weissman, A., Rotstein, Z., Manor, M., Hegesh, J., Anteby, E., Lipitz, S., and Achiron, R. (1997). Congenital heart defects: natural course an in utero development. *Circulation*.

Yu, A. C. H. and Cobbold, R. S. C. (2006). A matrix pencil estimator with adaptive rank selection: Application to in vivo flow studies. *IEEE Ultrasonics Symposium*.

Yu, A. C. H., Johnston, K. W., and Cobbold, R. S. C. (2007). Frequency-based signal processing for ultrasound color flow imaging. *Journal of the Canadian Acoustical Association*.

Yu, A. C. H. and Løvstakken, L. (2010). Eigen-based clutter filter design for ultrasound color flow imaging: A review. *IEEE Transactions on Ultrasonics, Ferroelectrics, and Frequency Control, vol. 57, no. 5*.